



# Three-dimensional high speed drop impact onto solid surfaces at arbitrary angles

Radu Cimpeanu\*, Demetrios T. Papageorgiou

Department of Mathematics, Imperial College London, London SW7 2AZ, United Kingdom

## ARTICLE INFO

### Article history:

Received 3 August 2017

Revised 20 March 2018

Accepted 18 June 2018

Available online 19 June 2018

### Keywords:

Drop impact

Stagnation-point flow

Spreading

Splashing

Volume-of-fluid

Direct numerical simulations

## ABSTRACT

The rich structures arising from the impingement dynamics of water drops onto solid substrates at high velocities are investigated numerically. Current methodologies in the aircraft industry estimating water collection on aircraft surfaces are based on particle trajectory calculations and empirical extensions thereof in order to approximate the complex fluid-structure interactions. We perform direct numerical simulations (DNS) using the volume-of-fluid method in three dimensions, for a collection of drop sizes and impingement angles. The high speed background air flow is coupled with the motion of the liquid in the framework of oblique stagnation-point flow. Qualitative and quantitative features are studied in both pre- and post-impact stages. One-to-one comparisons are made with experimental data available from the investigations of Sor and García-Magariño (2015), while the main body of results is created using parameters relevant to flight conditions with droplet sizes in the ranges from tens to several hundreds of microns, as presented by Papadakis et al. (2004). Drop deformation, collision, coalescence and microdrop ejection and dynamics, all typically neglected or empirically modelled, are accurately accounted for. In particular, we identify new morphological features in regimes below the splashing threshold in the modelled conditions. We then expand on the variation in the number and distribution of ejected microdrops as a function of the impacting drop size beyond this threshold. The presented drop impact model addresses key questions at a fundamental level, however the conclusions of the study extend towards the advancement of understanding of water dynamics on aircraft surfaces, which has important implications in terms of compliance to aircraft safety regulations. The proposed methodology may also be utilised and extended in the context of related industrial applications involving high speed drop impact such as inkjet printing and combustion.

© 2018 The Authors. Published by Elsevier Ltd.

This is an open access article under the CC BY license. (<http://creativecommons.org/licenses/by/4.0/>)

## 1. Introduction

Since the days of Worthington (1876), the problem of droplet impact has offered the fluid dynamics research community exciting opportunities and challenges over the course of its history. For the first time in a systematic manner, in his book entitled *A study of splashes* (Worthington, 1908), Worthington makes use of early photographic technology (alongside careful sketchwork) to provide a comprehensive visual interpretation of splashing phenomena. The framework has since captivated the interest of theoreticians and experimentalists alike, as it incorporates one of the most invitingly simple geometrical configurations, while at the same time giving rise to diverse and rich phenomena of immense scope.

\* Corresponding author.

E-mail address: [radu.cimpeanu11@imperial.ac.uk](mailto:radu.cimpeanu11@imperial.ac.uk) (R. Cimpeanu).

URL: <http://www.imperial.ac.uk/people/radu.cimpeanu11> (R. Cimpeanu)

A plethora of application areas benefit from understanding the outcomes of droplet impact events. We emphasise in particular the role of droplet splashing (or absence thereof) in printing technologies (van Dam and Le Clerc, 2004; Jung and Hutchings, 2012), combustion (Moreira et al., 2010), granular material interactions at all scales (Thoroddsen and Shen, 2001; Marston et al., 2012), electronics (Kim, 2007) and spray-cooling in nuclear reactors (Sawan and Carbon, 1975). The design of superhydrophobic coatings in relation to droplet impact dynamics (Tsai et al., 2009; Deng et al., 2009) is yet another prime example of the widespread applicability of this canonical problem.

Recent reviews provide an excellent insight into the state-of-the-art in the field within each decade (Rein, 1993 in the 1990's, Yarin, 2006 in the 2000's and more recently Josserand and Thoroddsen, 2016). The area has witnessed a very strong surge in the past decade, fuelled in part by the development of progressively more powerful imaging technologies, with both frame rates and resolutions capable of capturing details beyond the scope of

previous equipment (see Thoroddsen et al., 2008 as well). Furthermore, the improvement of numerical algorithms and usage of high performance computing has enabled computational studies that complement and inform both experimental and analytical work. We focus particularly on the volume-of-fluid package *Geris* (Popinet, 2003; 2009), which is one of the most popular open-source tools due to its strengths in dealing with interfacial flows on a range of very different scales. Comparisons with experiments, as well as analytical work have been consistently robust, be it in cases of liquid-liquid impact (Thoraval et al., 2012; Agbaglah et al., 2015) or impacts of liquid onto solid surfaces (Visser et al., 2015; Philippi et al., 2016; Wildeman et al., 2016).

In the case of normal (perpendicular) impact at low-to-moderate velocities (and depending on specific fluid properties), an axisymmetric assumption can be used in analytical and computational investigations. The reduction in dimensionality is a significant advantage that has led to very efficient (axisymmetric) computations and good agreement with experiments. Visser et al. (2015) for example, while innovating experimental technology enabling the time-resolved investigation of micron-sized drop impacts, have managed to conduct successful comparisons with direct numerical simulations at impact speeds of up to 50 m/s, a regime which is commonplace in combustion, inkjet printing or aircraft-related applications. In the respective scenario, the small drops spread onto the surface in what is known as pancaking motion, with the axisymmetric approximation remaining valid in the absence of splashing events.

In cases where spreading and later retraction rather than splashing occurs, the vast majority of efforts have been dedicated towards identifying quantities such as the maximal spreading radius (Stow and Hadfield, 1981; Clanet et al., 2004; Fedorchenko et al., 2005; Roisman, 2009; Schroll et al., 2010) and most recently Wildeman et al. (2016), as well as the resulting minimal film thickness, retraction dynamics and the role of the internal boundary layer - see Bartolo et al. (2005) and in particular Eggers et al. (2010) for a comprehensive investigation of the above.

At higher speeds however, there is still an ongoing debate as to how the splashing phenomena are first initiated, and the splashing threshold in particular. Up until the groundbreaking experimental investigation of Xu et al. (2005), there have been numerous attempts to characterise the transition from spreading to splashing dynamics in the classical impact problem in terms of drop-related parameters only (size, density, viscosity, surface tension coefficient, impact velocity). The Chicago group discovered, however, that decreasing the ambient air pressure may completely suppress splashing. As such, a host of additional modelling, experimental and numerical efforts have been initiated, with the work of Riboux and Gordillo (2014) proposing a model deducing a threshold splashing velocity as a function of a generalised set of key parameters containing the liquid density and viscosity, the drop radius, gas density and viscosity, the interfacial tension coefficient, as well as the nanometric mean free path of the gas molecules.

Once the drop splashes, there is very little attention dedicated to the ensuing dynamics, with the sizes and velocities of secondary drops being prohibitively small experimentally and computationally, although advances have taken place recently in terms of simplified models. In particular, Riboux and Gordillo (2015) have proposed a one-dimensional approach to predicting sizes and velocities of ejected droplets for  $\mathcal{O}(1)$  mm sized impacting drops and low speeds, finding reasonable agreement with experiments.

As underlined by Jossier and Thoroddsen (2016), there are several exciting challenges lying ahead, two of which are of great importance in the context of the present work. First of all, gaining an improved understanding of splashing, particularly in difficult high speed conditions of industrial relevance, is moving more and more within reach, and further detailed investigation using

the available tools is needed. Secondly, oblique impacts are rarely analysed (exceptions being Mundo et al., 1995; Sikalo et al., 2005; Bird et al., 2009) due to the additional flow complexity. Most often, qualitative rather than quantitative phenomena are explored in detail. The exceptions tend to focus on large scale effects at the level of the entire drop, as opposed to details at the level of the splashing itself and the interesting local structures arising. Both of these themes lie at the heart of the present work, which focuses on the modelling and computation of oblique three-dimensional drop impact in aerodynamic conditions.

In aircraft-oriented research and design involving drop impact, the relevant scales are often dictated by the size of the parts that are most affected by phenomena such as water impingement, retention and finally icing and its prevention. The wings or nacelles are several metres long, while computing accurate air flows around them requires domains that span tens of metres in all dimensions. This becomes highly prohibitive in terms of accurate resolution of the intricate and sensitive physical effects pertaining to drop impact, which often happen at sub-micron scales in the order of tens to hundreds of microseconds. As such, particle-trajectory calculations of various degrees of complexity have thus far proven to be the only tractable solution in industrial setting.

There are several important limitations of current models, as pointed out by Gent et al. (2000) in a relatively recent review:

- droplets are assumed to be spherical and non-deformable as they approach the solid surface, hence topological transitions such as the emergence of secondary drops either before or after impact are not considered;
- phenomena related to multiple drops such as collisions are completely ignored;
- aerodynamic drag, gravity and buoyancy are assumed to be the sole forces affecting the drop trajectories;
- whereas the local velocity of the air flow is embedded into the ordinary differential equations governing the updates in drop trajectories, the liquid mass is assumed not to affect the surrounding air flow;
- once on the surface, empirical models translate the drop contribution towards liquid film formation and its movement further downstream along the surface of interest.

Many of these assumptions become inaccurate in the context of the large supercooled droplets (larger than several tens of microns) found in the atmosphere. The difficulties outlined above have yet to be overcome, and most modelling is performed at a highly coarse-grained level (Potapczuk et al., 1993; Bragg, 1996; Rutkowski et al., 2003; Wright and Potapczuk, 2004; Wright, 2005; 2006; Honsek et al., 2008; Bilodeau et al., 2015), with semi-empirical relations of varying complexity being proposed in order to match with the rich but ultimately limited experimental data available by NASA experiments conducted by Papadakis et al. (2003, 2004). The focus here is primarily on the final water retention values rather than the more fundamental problem of the detailed impact process, making it ideal from an engineering standpoint but offering limited insight into the underlying physics. In the past few years, the group at INTA/Madrid (Vargas et al., 2012; Sor and García-Magariño, 2015) have looked in more detail into the deformation of large-scale drops prior to impact, with results that indicate regimes far more complex than captured by the typical assumptions mentioned above. Several studies focusing on recent numerical advances in the high speed regime ( $> 50$  m/s impact velocity) have emerged, particularly for impacts onto liquid, but also onto solid surfaces (Ming and Jing, 2014; Cheng and Lou, 2015; Guo et al., 2016; Cherdantsev et al., 2017; Xie et al., 2017). These offer exciting opportunities to study short timescale phenomena beyond the reach of traditional particle methods, however up to this point there have been few attempts to integrate the drop impingement

process into a framework that includes a more realistic model for the movement and effect of the air flow around the bodies of interest.

The present work bridges the relevant scales in the problem of drop impact onto aircraft surfaces and proposes a suitable model for the air flow around the solid bodies of interest in which we then accurately resolve the drop impingement process. While the drops are initialised as spherical sufficiently far away from the body, we characterise their deformation prior to impact and the spreading/splashing thereafter, depending on drop sizes and angles of impingement. We focus on the asymmetric features of the drop spreading when droplets are very small (less than a few tens of microns), phenomena which to our knowledge have yet to be observed. As the drop size increases, we quantify the sizes and positions of the secondary drops emerging as a result of the impingement and provide useful metrics for practitioners looking to improve water retention calculation methodology and a deeper understanding of the physics involved in the impact process under challenging conditions. All flow parameters have been carefully chosen to match with previous experimental studies or known flight-specific values, while many of the quantified metrics are also compared to classical theoretical results where applicable.

The investigation is structured as follows. We introduce the proposed mathematical model in Section 2, followed by a detailed description of the computational framework in Section 3. We then analyse our findings in Section 4, focusing on both pre-impact dynamics in Section 4.1 and post-impact dynamics in Section 4.2. These results are discussed and placed into context in Section 5, followed by concluding remarks.

## 2. Mathematical model

In the present section we elaborate on how we adapt the classical problem of drop impact to the high speed flow conditions of interest around aircraft surfaces. First we discuss some useful assumptions allowing us to reduce geometrical complexity in the problem in Section 2.1, after which we expand on the mathematical model itself, outlining the relevant equations, initial and boundary conditions.

### 2.1. Scale transition

The full model geometry discussed in previous paragraphs (aircraft wings/fuselage components) is far too complicated - and specific - from many points of view. To begin with, our aim is to present a general methodology, applicable to a number of surfaces rather than a specific specialised geometry. Secondly, the multi-scale modelling of both the background air flow around the large scale body and the splashing dynamics within the much smaller drop impact regions is beyond reach in terms of theoretical and current computational resources. We thus employ several simplifications to enable a closer inspection of a much more amenable problem, which still preserves the main physical characteristics we wish to address.

Based on the disparity between the two scales in the problem (the impacting droplet diameter and the solid body it impinges upon), we assume the curvature of the body to have negligible effects. To justify this approximation, the radius of curvature of the leading edge of a typical NACA airfoil or nacelle lipskin, the most sensitive regions to water retention and icing, is estimated to be of  $R_b = \mathcal{O}(10^{-1})$  m for standard commercial aircrafts. For a reasonably large droplet of radius  $R = 100$   $\mu\text{m}$ , we find  $R/R_b \approx 10^{-3}$ . Thus, from the perspective of modelling the local droplet impact, the surface can be considered as approximately flat. From a different viewpoint, we zoom in sufficiently close to the surface of the

solid body, such that in the respective region the droplet diameter is the representative lengthscale and hence the details of the impact can be carefully examined.

### 2.2. Governing equations

The framework of studying these fluids as incompressible in laminar flow conditions is a natural choice in the context of our problem, as the primary target flight regimes of take-off and landing are characterised by relatively low velocities compared to those reached at higher altitudes. Furthermore, most droplet impingement events are concentrated close to the leading edge of the geometries of interest, where the flow has yet to enter the transition from laminar to turbulent state. Even in such circumstances, a complex and likely empirical turbulence model would prevent the inspection of the detailed liquid dynamics, which is the main goal of the present investigation.

The model fluids are assumed to be incompressible, immiscible and viscous. Subscript 1 is used to refer to the fluid inside the drop (taken to be water), whereas subscript 2 decorates quantities in the surrounding (air) flow. Let  $\rho_{1,2}$  and  $\mu_{1,2}$  denote the constant densities and dynamic viscosities of the two fluids in the system. The constant surface tension coefficient at the interface is given by  $\sigma$ . Velocity vectors  $\mathbf{U}_{1,2} = (U_{1,2}, V_{1,2})$  and pressures  $P_{1,2}$  are used in the formulation of the dimensional momentum and continuity equations

$$\rho_1(\mathbf{U}_{1t} + (\mathbf{U}_1 \cdot \nabla)\mathbf{U}_1) = -\nabla P_1 + \mu_1 \Delta \mathbf{U}_1, \quad (1)$$

$$\rho_2(\mathbf{U}_{2t} + (\mathbf{U}_2 \cdot \nabla)\mathbf{U}_2) = -\nabla P_2 + \mu_2 \Delta \mathbf{U}_2, \quad (2)$$

$$\nabla \cdot \mathbf{U}_{1,2} = 0. \quad (3)$$

Gravitational forces are assumed to be negligible. There are two lengthscales in the problem: the droplet diameter  $D$ , the natural choice for the reference lengthscale, and the size of the (finite) computational domain  $L$ . We scale lengths by  $D$ , velocities by a reference background velocity  $U_\infty$  and pressures by  $\rho_1 U_\infty^2$ . The emerging non-dimensional parameters are

$$\text{Re} = \rho_1 U_\infty D / \mu_1, \quad \text{We} = \rho_1 U_\infty^2 D / \sigma, \quad K = \text{We} \sqrt{\text{Re}} = \sqrt{\rho_1^3 D^3 U_\infty^5 / (\sigma^2 \mu_1)}. \quad (4)$$

The Reynolds number  $\text{Re}$  and Weber number  $\text{We}$  appear directly from the non-dimensionalisation procedure, while the splashing parameter  $K$  is introduced as an intrinsic element of a drop impact problem. The expression, originally introduced by [Stow and Hadfield \(1981\)](#), has been used to classify the possible outcomes of the impact. This parameter has been controversial in the literature and cannot independently account for the classification of the complicated impact process (see [Xu et al., 2005](#); [Mandre and Brenner, 2012](#)), however it serves as an indicator of the force of the splashing and permits comparisons with previous investigations.

We also introduce density and viscosity ratios

$$r = \rho_1 / \rho_2, \quad m = \mu_1 / \mu_2, \quad (5)$$

and non-dimensionalise the governing Eqs. (1)–(3), resulting in

$$\mathbf{u}_{1t} + (\mathbf{u}_1 \cdot \nabla)\mathbf{u}_1 = -\nabla p_1 + \text{Re}^{-1} \Delta \mathbf{u}_1, \quad (6)$$

$$\mathbf{u}_{2t} + (\mathbf{u}_2 \cdot \nabla)\mathbf{u}_2 = -r \nabla p_2 + r m^{-1} \text{Re}^{-1} \Delta \mathbf{u}_2, \quad (7)$$

$$\nabla \cdot \mathbf{u}_{1,2} = 0. \quad (8)$$

The non-dimensional timescale is  $D/U_\infty$ . Typical fluid properties in the case of water and air at near freezing temperature (close to 0°C) are given as follows. Water has density  $\rho_1 = 999.8 \text{ kg/m}^3$  and dynamic viscosity  $\mu_1 = 1.16 \times 10^{-3} \text{ kg/ms}$ , while the air density is  $\rho_2 = 1.21 \text{ kg/m}^3$  and its dynamic viscosity  $\mu_2 = 1.81 \times 10^{-5} \text{ kg/ms}$ . The constant surface tension coefficient is  $\sigma = 7.2 \times 10^{-2} \text{ N/m}$  and a representative value for the velocity of the background flow is  $U_\infty = 78.44 \text{ m/s}$ . This value has been selected to coincide with classical experimental investigations (Papadakis et al., 2004), as well as subsequent numerical investigations in the aerospace engineering community (e.g. Bilodeau et al., 2015). We underline the large density ( $r = 826.28$ ) and viscosity ( $m = 64.09$ ) ratios, which pose significant numerical challenges - these are touched upon in Section 3. Tables 1 and 2 in the results discussion indicate the values of the key dimensionless groups in the problem and highlight the violent high speed impact regime investigated here.

To define the interfacial conditions governing the motion of the drop, we assume a sharp interface  $y = S(x, t)$ ; subsequently this is relaxed in the context of the volume-of-fluid methodology employed in the direct numerical simulations. The prescribed interfacial conditions are, in order, the kinematic condition, the continuity of normal and tangential stresses, and continuity of velocity components:

$$w_i = S_t + u_i S_x + v_i S_y, \quad i = 1, 2, \quad (9)$$

$$[\mathbf{n} \cdot \mathcal{T} \cdot \mathbf{n}]_2^1 = \text{We}^{-1} \kappa, \quad (10)$$

$$[\mathbf{t} \cdot \mathcal{T} \cdot \mathbf{n}]_2^1 = 0, \quad (11)$$

$$[\mathbf{u}]_2^1 = 0, \quad (12)$$

where  $[(\cdot)]_2^1 = (\cdot)_1 - (\cdot)_2$  represents the jump across the interface,  $\mathbf{n}$ , and  $\mathbf{t}$  are the unit normal and tangent to the interface, respectively, and  $\kappa$  is the interfacial curvature. The stress tensor  $\mathcal{T}$  is given by

$$\mathcal{T}_{ij} = -p\delta_{ij} + \mu \left( \frac{\partial u_i}{\partial x_j} + \frac{\partial u_j}{\partial x_i} \right), \quad (13)$$

where the appropriate subscript is used in different fluid regions. The initial and boundary conditions for the finite computational domain are described in the following subsection.

### 2.3. Background flow

One of the most important features of the model is the interaction between the liquid drop and the air around it. In typical experimental conditions, droplets are formed at the tip of an injection device and fall under gravity, with the height of the device being varied in order to adjust the terminal velocity and hence fix the relevant dimensionless parameters. In order to reach velocities beyond  $\mathcal{O}(1) \text{ m/s}$  it is necessary to have some form of ejection mechanism that ensures not only reproducibility of the shapes, but also a stability of the dynamics in early stages as the drop travels through the quiescent air flow and may become immediately sheared and violently deformed and broken up. As such, most of the investigations concerning velocities above  $10 \text{ m/s}$  are restricted to very small drops (well below  $100 \mu\text{m}$ ), such that surface tension is strong enough to preserve the approximately spherical shape of the drop.

In flight conditions, leading edge droplet impact can be locally embedded in a stagnation-point flow which develops into boundary layers on either side of the geometry. As such, most droplets encounter a developing boundary layer structure with a

strong shear component. In an effort to reproduce the same type of air flow environment while preserving generality, we proposed an oblique-stagnation point flow model for the air flow, with the liquid drop being seeded sufficiently far away from the body on the dividing streamline of the flow. The reasons behind this choice are twofold:

1. Far away from the surface the drop should retain its shape and setting a uniform velocity field inside the drop with a zero (as in most desktop experiment setups) or purely horizontal (along the body) air motion would produce instantaneous breakup of the drop. The choice for stagnation-point background flow and the initial position of the drop ensures that the air flow undergoes only small changes until sufficiently close to the surface, which is when we expect the drop to start deforming in real life conditions.
2. The stagnation-point flow has the same characteristics in the near vicinity of the point of zero velocities as on the aircraft surface, in that boundary layers are developing on either side of it and growing as we move further downstream. As such the liquid drop is subjected to the shear flow naturally occurring above the solid surface. This is best represented in the highly oblique impact cases, in which the air flow streamlines near the surface have strong deviations from their far-field orientation. Oncoming drops depart from their host streamlines close to the surface and their final impingement points are well within the boundary layer growth region. The choice in initial positioning of the drop thus retains generality, while at the same time providing suitable conditions for the early stages of the drop dynamics.

There are however several points to be made prior to advancing to the mathematical description of the model. First of all, the dynamics of drops in uniform flow has been extensively investigated and the deformation characteristics for large enough drops are very rich (see Jalaal and Mehravaran, 2012 for a recent computational study). Therefore, even in the case of tailoring the initial position of the drop to a region of uniform air flow, the drop is anticipated to suffer significant deformations as it moves towards the solid body. The size of the finite computational domain can then be used to alleviate (or enhance) this effect. Secondly, it should be noted that there still remains a fundamental difference to the practical scenario in which a solid body is moving through high liquid water content clouds (with stationary water drops of varying sizes) as opposed to drops impinging onto a static solid surface, as in the present case. Here we are enhancing the inertial contribution in the pre-impact drop dynamics and our choice in initial position of the drop does ultimately affect the liquid volume impinging onto the surface. Previous experimental results have however been used as guidance in order to best account for the complex flow dynamics, while retaining a suitable well-controlled flow environment.

With the above properties in mind, we underline that the background air flow poses its own non-trivial challenges. The history of the problem dates back to Hiemenz (1911), who was the first to present a solution for the two-dimensional normal stagnation point flow. Howarth (1951) then extended the formulation to three dimensions. The oblique case was first touched upon by Stuart (1959), then later rediscovered independently by Tamada (1979) and Dorrepaal (1986). There have been a number of corrections, extensions and generalisations on the main problem, for example by Wang (2008) and Tooke and Blyth (2008), including extension to two-fluid systems (air flow impinging onto liquid films above a solid surface), as studied by Tilley and Weidman (1998) and Blyth and Pozrikidis (2005). As far as we know there is no general analytical solution to the three-dimensional stagnation-point flow problem at an arbitrary angle. As such, we attempt to recreate this type of flow numerically using a combina-



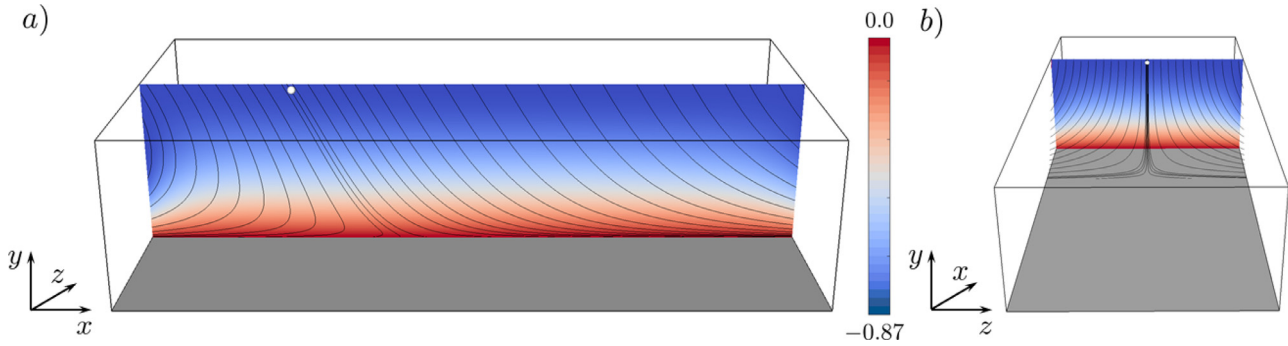


**Fig. 1.** Snapshots of the converged background velocity field obtained as a result of imposing uniform flow boundary conditions at an angle of  $\theta_i = 60^\circ$  on the upper boundary, hitting a flat solid surface at the bottom, with outflow conditions on all lateral boundaries. The two cross-sections through (a) the central  $x-y$  plane and (b) the  $y-z$  plane illustrate the vertical velocity field (negative above, zero due to no-slip on the surface), as well as streamlines of the flow. The water drop, shown in white, is initialised on the dividing streamline near the upper border of the geometry.

tion of suitable boundary conditions that preserve its main characteristics in the interior of the domain.

The three-dimensional computational box is selected to be of size  $4L/D \times L/D \times 2L/D$  in  $(x, y, z)$ -directions, where  $L/D$  is taken to be of size 20, i.e. 20 drop diameters. The flat solid surface is taken to be in the  $(x, z)$ -plane, with no-slip and impermeability conditions prescribed in this region, such that at  $\mathbf{u}_{1,2} = 0$  at  $y = 0$ .

In order to model the oncoming flow at an arbitrary angle of incidence  $\theta_i$  we prescribe inflow conditions given by

$$u_2(x, L/D, t) = \cos(\theta_i), \quad v_2(x, L/D, t) = -\sin(\theta_i) \text{ at } y = L/D. \quad (14)$$

Laterally we impose typical free outflow conditions on all remaining four sides of the box. The main reason for doing so relates to the movement of the secondary drops resulting as a consequence of the splash which cause perturbations in the flow field, making it difficult to fix velocities at the boundaries. The initial conditions are set to

$$u_2(x, y, 0) = \cos(\theta_i), \quad v_2(x, y, 0) = -\sin(\theta_i), \quad (15)$$

prompting the need for the convergence of the background flow to a steady state prior to the inclusion of the liquid droplets into the computational domain. For all cases considered in the present investigation, an evolution of the flow spanning 100 dimensionless time units proved more than sufficient for this purpose, with a tolerance of  $10^{-6}$  in the components of the velocity field selected to verify flow convergence to steady state. We have confirmed this for all angles of incidence using a root mean square norm of the velocity field, presented in Fig. 2(b). Time  $t = 0$  is taken to be the time at which the drop is seeded inside the domain and by this convention the direct numerical simulations begin at  $t = -100$ .

Focusing on the mid- $(x, y)$ -plane (at  $z = 0$ , see Fig. 1(a)), we find similar flow properties to the classical case of oblique stagnation point-flow in two dimensions. Using the typical definition for the stream function  $\psi(x, y)$ , where the horizontal velocity component  $u = \psi_y$  and the vertical velocity component  $v = -\psi_x$ , sufficiently far away from the wall the flow takes the form

$$\psi(x, y) = kxy + \frac{1}{2}\zeta y^2. \quad (16)$$

This is effectively a superposition of irrotational stagnation-point flow of strength  $k$  and a uniform shear flow parallel to the solid surface (in the  $x$ -direction), where  $k$  and  $\zeta$  are scale constants (see Blyth and Pozrikidis, 2005 for a recent exposition on this scenario).  $\psi = 0$  denotes the dividing streamline onto which the liquid drop is initialised just below the upper boundary of the three-dimensional domain, with its centre at  $y = 19.25$  and  $z = 0$  and with  $x$  varying as a function of the angle of incidence  $\theta_i$  of the

background flow. Fig. 1(a) provides a visualisation of the converged flow field at the instance of the initialisation of the drop for the case when  $\theta_i = \pi/3$ .

We underline that, despite the flow being essentially two-dimensional in the upper part of the domain (below the inflow boundary), due to the presence of the solid surface and the lateral outflow condition, it develops its full three-dimensional structure close to the impingement region, with a single stagnation point being present in the flow irrespective of the impingement angle. This is best observed in Fig. 2(a), but also in Fig. 1, where streamlines are drawn on top of velocity fields (illustrated in colour) plotted in different two-dimensional cross-sectional planes to indicate the deflection in the air flow.

Once the background air flow has reached its steady state, the initially spherical liquid drop is prescribed to enter the computational domain at a desired location  $(x_i, y_i = 19.25, z_i = 0)$ . The drop then inherits the local velocity field of the background air flow which is an approximately uniform flow directed towards the surface at an angle  $\theta_i$ , and is advected towards the solid surface. The droplet shape is subject to physical deformations up to the time of its impact. Full hydrodynamic coupling determines its trajectory and shape, with no further assumptions being made beyond this point.

### 3. Numerical methodology

The numerical computations in the present study have been carried out using the open-source package *Gerris* (Popinet, 2003; 2009) (<http://gfs.sourceforge.net/>), which has been used extensively with great success by the multi-phase flow community over the last decade. The package is ideal for our purposes since it accurately solves the incompressible Navier–Stokes equations (and a variety of additional multi-physics extensions) using the finite volume method and a volume-of-fluid approach to account for fluid-fluid interfaces. The schemes are second order accurate in both space and time, with strong adaptive mesh refinement capabilities ensuring the computational cost remains relatively low even in challenging multi-scale contexts such as those in the present problem. In the following paragraph we elaborate on some of the specific measures used to ensure a good numerical performance, and also underline the overall features of our extensive computational effort.

The large density ratio (recall that for water-air flows  $r = 826.281$ ) between the fluids may cause convergence issues for multi-grid Poisson solvers as the one used in *Gerris* (Tryggvason et al., 2011), causing slow convergence or leading to a breakdown of the numerical solution altogether. A smoothing operator/filter has been proposed (Popinet, 2009; Fuster, 2013) in order

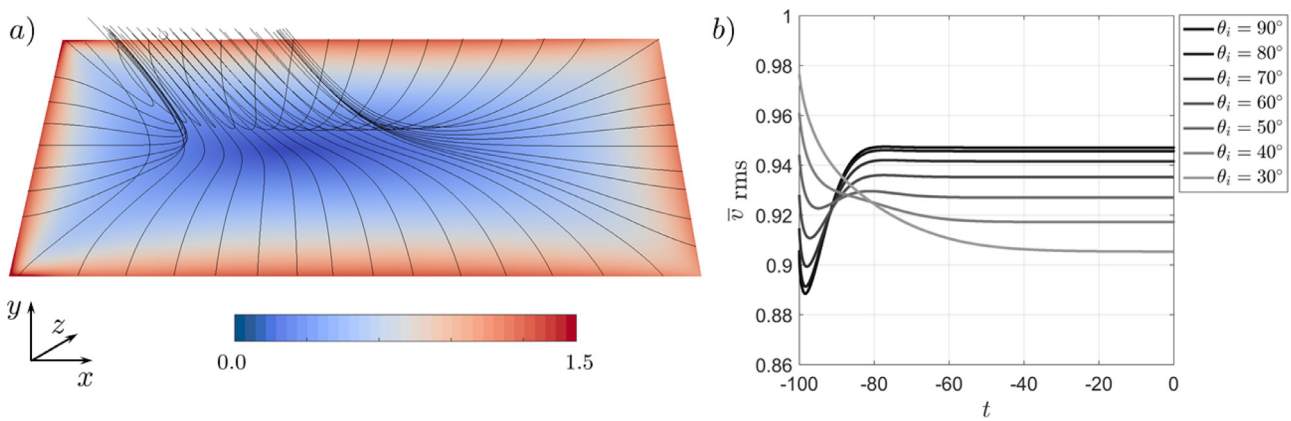


**Fig. 2.** (a) Magnitude of velocity vector on an  $x-z$  plane immediately above the surface, at  $y = 0.01$ . A single stagnation point is visible in the centre of the computational box, with streamlines aiding the visualisation of the flow as it increases in velocity towards the lateral boundaries. (b) Root-mean-square norm of the velocity vector for different angles of incidence  $30^\circ \leq \theta_i \leq 90^\circ$  of the background air flow.

to alleviate this. Spatial filtering consists of averaging over the corners of a computational cell (four in 2D and eight in 3D), which are in turn obtained by averaging the centred values of the corner neighbours. Applying the filter effectively smoothes the representation of the interface over a larger number of cells and can be applied any number of times, although previous investigations on drop impact argue that a single iteration of the filtering operator is sufficient (Thoraval, 2013). As a result of this manipulation, the errors are maintained at a reasonable (and controllable) magnitude, while the convergence properties of the solver are much improved.

The qualities of the package, in particular in terms of adaptive mesh refinement (AMR), become evident in the study of the problem of drop impact at high velocities. The background air flow requires a strong level of refinement close to the surface of the solid body to account for the presence of the developing boundary layers around the stagnation point of the flow. At the same time, capturing the evolution of the fluid-fluid interface demands an appropriate resolution, enabling possible topological transitions. Splashing entails the creation and subsequent tracking of a large number of secondary droplets, which may or may not coalesce with other bodies of fluid. In addition, suitable choices for refinement with respect to sharp changes in vorticity were also implemented. We also note the more stringent treatment required during touchdown, in which a reduced timestep and an extended local refinement region is necessary to avoid numerical artefacts. The computational gain when comparing to the case of a uniform mesh is remarkable. The large domain would require  $\mathcal{O}(10^{10-11})$  grid cells at the finest resolution, however with the use of the adaptive mesh refinement this is decreased several orders of magnitude down to  $\mathcal{O}(10^6)$  degrees of freedom, which becomes significantly more tractable. Many of the results presented would have reached considerable runtimes (as well as challenging memory and data storage requirements) without the usage of adaptive mesh refinement, and possibly making many of the calculations presented here unrealisable.

We also employed the functionality to selectively eliminate droplets and bubbles whose dimensions are below a threshold number of grid cells (chosen to be 16), thus fixing the minimum lengthscale that computations can account for. Note that this is already well within the sub-micron scale. This feature becomes useful when secondary droplet break-off is violent and causes the fragmentation of the fluid into droplets of a very small size which suffer from geometrical reconstruction errors as a result of them spanning a small number of grid cells in each dimension. In practice the technique works by replacing the connected volumes (under a specified size) containing the drop fluid phase (water in our case) with the background fluid (air). Furthermore, in our imple-

mentation complete droplet removal takes place if the droplets are found within one spatial unit of lateral boundaries, in order to limit numerical artefacts when encountering the outflow region, or sufficiently high above the surface of the solid body ( $y > 10.0$ ), to avoid high speed secondary droplets reaching the inflow boundary and causing numerical instabilities. In practice, the mentioned situation can be avoided by prescribing a larger computational domain that demands increased computational costs. The selective removal of droplets ensures that a geometry of manageable size can still be used reliably. The flow in the vicinity of the impact region is unaffected by this treatment restricted to the near-lateral boundary regions, hence no flow information is artificially lost.

Many of the problems of interest require the treatment of a triple contact point between the solid surface and the liquid-gas interface. We note that the default mesh-dependent static contact angle model with a selected value of  $90^\circ$  is used here. The limitations of this basic method, as well as proposed improvements have been recently discussed by Afkhami et al. (2009), who introduced a versatile dynamic contact angle model (implemented in an extension of Gerris). In a related context, Pasandideh-Fard et al. (1996) note that the inertially dominated stages of the flow are unaffected by changes in the contact angle, which had been altered with the use of surfactants in their investigation. In general, the suitability of the static contact angle model in the inertia-dominated spreading regime has been studied extensively (Yokoi et al., 2009; Guo et al., 2016) and the present choice is not restrictive. We have experimented numerically with both grid sizes and different imposed static contact angle values in two dimensions, confirming that in the early stages of the impact we are in a regime which is insensitive to the choice of contact angle at the wall.

The runs in the present study have been performed at multiple resolution levels, varying from  $2^{10}$  to  $2^{12}$  grid cells per spatial dimension in each computational box. As the interfacial shape is set to be resolved at this level, this would translate to up to approximately 200 cells per diameter for the initial spherical drop. Before impingement we do not require such levels of refinement away from interfaces. On the other hand, right before, during and after impingement, the entire liquid volume demands a strong refinement level. Despite these stringent requirements, with the chosen settings and drop sizes, each finest resolution cell spans from  $0.097 \mu\text{m}$  for the smallest impinging drops studied to  $1.15 \mu\text{m}$  in the case of the largest drops of initial diameter of just over  $230 \mu\text{m}$ . These levels have been selected to provide as much detail at the micron and sub-micron levels as possible. Many features, such as for example the minimal film thickness arising as a result of the spreading of a drop on the surface, have well-established sizes

which are useful guidelines for what scales need to be captured and are used for comparisons and validation. From a more general standpoint, for the decision on a suitable level of refinement and mesh adaptivity setting we have relied on three main criteria: (a) mass conservation; (b) changes in defined metrics such as velocity and vorticity norms, secondary drop size distribution etc. and (c) comparisons to available analytical predictions and experimental data in the literature. Once all three criteria have been met, the configuration in question was propagated towards full parameter studies over the variables of interest. We emphasise that for the top two levels of refinement, volume conservation is accurate to within 1% across the entire set of tests in the present work, with only the most challenging of test cases (the largest initial drop diameter prescribed) causing errors of the order of 3–4% a combination of the difficult conditions (high  $Re/We$ ) and the selective drop removal mechanism introduced above, with smaller scale features being more frequent in this scenario. A typical computation under these conditions requires in excess of  $2 \times 10^3$  CPU hours for the lowest resolution tested and approximately  $10^4$  CPU hours for the more refined cases.

In the next section we describe, in turn, our computational results for pre-impact deformation and post-impact dynamics, concentrating on both fundamental phenomena and aspects related to the larger scale system itself.

#### 4. Results

Once the drop is initialised in the steady background flow, it travels towards the surface guided by an initially uniform (but  $\theta_i$ -dependent) velocity field, with streamlines deforming as the solid surface is approached. Analysing the deviation from the initially spherical shape as a function of time is one of the primary goals of the present work, since, as noted earlier, this effect is often overlooked in standard water retention calculation models.

In order to provide a suitable validation framework for the present results, we have tailored the parameters to coincide with a subset of the data of the only experimental investigation of the pre-impact deformation and break-up phenomena we are aware of - see Vargas et al. (2012) and Sor and García-Magariño (2015). Therein, an experimental setup consisting of a monosize droplet dispenser, a rotating arm with a model wing fixed at its end, as well as associated motor and camera equipment are used to capture the drop dynamics as the solid body approaches the liquid droplets at velocities of up to 100 m/s. As a result of the very violent regime, the size variation for the drops is restricted to  $D = 300 \mu\text{m}$  and above. Very few pixels per drop diameter are visible below this threshold and the resulting images can no longer be comprehensively analysed. As a consequence, in the results that follow we have selected three values within the respective range, as well as one smaller drop, typical of the sizes found in the high liquid water content regions aircraft travel through. The drop sizes, as well as all other associated dimensionless parameters are summarised in Table 1, where we underline that we have used a reference velocity of  $U_\infty = 90 \text{ m/s}$  (the same as in the main series of experiments Sor and García-Magariño, 2015) and the physical properties of water and air at relevant near freezing temperatures.

Following impact itself, depending on the relevant parameters, the drop is anticipated to either spread due to its momentum and subsequently recede under surface tension effects, or, in the cases of the larger drops, to splash and break up into secondary droplets which move away from the surface but may later re-impinge. Droplets found in the atmosphere typically lie within the interval of 20–250  $\mu\text{m}$  in diameter and as a consequence water catch studies reported in the literature (Papadakis et al., 2003; 2004; Wright, 2005; 2006; Honsek et al., 2008; Bilodeau et al., 2015) are found in this regime. We consider four test cases ( $D = 20, 52, 111, 236 \mu\text{m}$ )

for complete analysis of pre- and post-impact dynamics, in order to facilitate comparisons with results in the field and provide further insight under flight conditions of practical interest. The complete list of parameters is provided in Table 2, where the same water-air configuration is used, however this time with reference velocity  $U_\infty = 78.44 \text{ m/s}$ , in agreement with datasets discussed in previously mentioned studies.

For the smallest 20  $\mu\text{m}$  drops we consider an extensive parameter study in terms of impingement angles  $10^\circ \leq \theta_i \leq 90^\circ$  in increments of  $10^\circ$ . This enables a detailed analysis of the effects related to the competition between inertial and capillary regimes, while noting the influence of the background flow on the drop dynamics. For the more challenging larger droplets we focus on two specific cases, namely  $\theta_i = 60^\circ$  and  $\theta_i = 90^\circ$ , guiding us towards results in both symmetric and asymmetric impact, described in full detail in Section 4.2.

##### 4.1. Pre-impact dynamics

In the present subsection we describe qualitative and quantitative features related to the motion of droplets prior to them impacting the solid surface. Intuitively we expect the most deformation and possible break-up to happen close to the solid surface as the air flow slows down and the droplet encounters developing boundary layers. We note however that, particularly for large drops, a rich dynamics characterised by so-called bag break-up and rupture can be observed even in the case of simple uniform flow and in the absence of any streamline deflection (Jalaal and Mehravaran, 2012). These strongly time-dependent morphological changes underline the importance of one of the parameters in the presented model, namely the initial position of the drop relative to the solid surface. If prescribed too far away from the surface, the initial spherical drop may become completely fragmented by the time it reaches the surface, while seeding it too close to the surface may not allow sufficient time for its natural dynamics to occur before impingement. As such, the comparison to the experimental results from INTA/NASA (Vargas et al., 2012; Sor and García-Magariño, 2015) serves as an important validation step. The authors focused on describing and modelling the change in shape, as well as the consequences thereof in terms of predicting the drag coefficient of the evolving shape. They found that for moderate-sized droplets (with diameters in the hundreds of microns) the approximation of the shape as an oblate spheroid proves to be reasonably accurate, quantifying this deformation as  $a(t)/R$ , where  $a(t)$  denotes the evolving major semi-axis of the spheroid, normalised by the initial drop radius. This value was reported to increase smoothly from 1.0 as the drop is sufficiently far away from the surface to values in the range of 1.3 for  $D = 362 \mu\text{m}$ , to 2.0 for  $D \approx 1 \text{ mm}$ , increasing monotonically as a function of the size of the initial drop. As they approach the surface, the larger drops suffer considerable deformations in which the symmetric framework postulated before is no longer applicable. Finally, when close to within 10 mm of the solid surface, the drops violently break up into a cloud of secondary droplets which can only be described qualitatively in the experiments.

Example evolutions of the droplet shapes are shown in panels (a) and (b) of Fig. 3, in which we analyse the deformation of a relatively small drop ( $D = 362 \mu\text{m}$ ), as well as a large drop ( $D = 1048 \mu\text{m}$ ) alongside their experimental counterparts. In the former case, we find that the proposed mild deformation into an oblate spheroidal shape is recovered and good qualitative agreement with the experiments is found. The same applies for the latter larger drop case, in which the flattening of the shape is much more pronounced and asymmetric features arise in the latter stages. Note how the centre of gravity of the shape shifts towards the lower part of the drop in the third subimage, only to develop

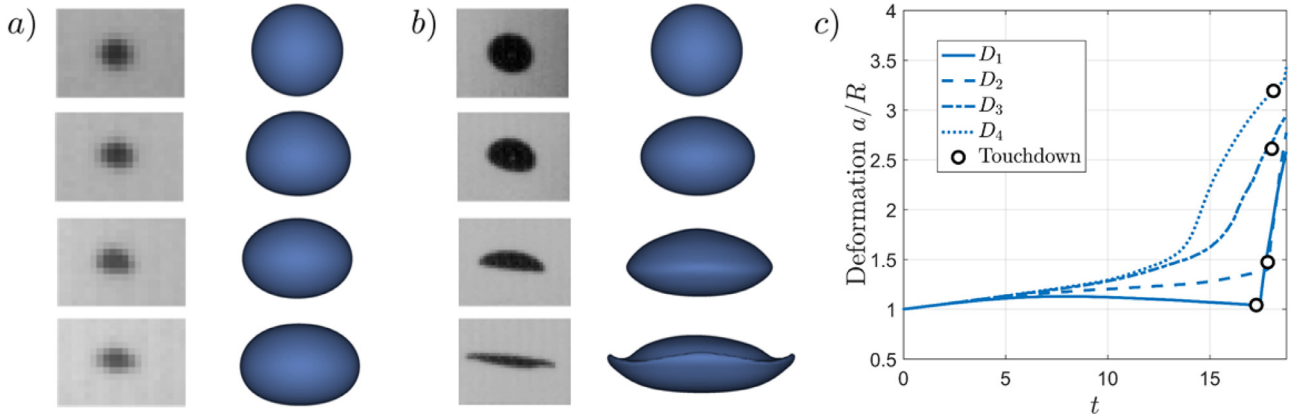


**Fig. 3.** Pre-impact drop deformation visualisation for spherical drops of diameter (a)  $D = 362 \mu\text{m}$  and (b)  $D = 1048 \mu\text{m}$ . Inside each panel the left images are experimental results by Sor and García-Magariño (2015), while the right images are the corresponding DNS results. The images are reproduced with permission by Instituto Nacional de Técnica Aeroespacial. (c) Quantification of the drop deformation in terms of the drop semiaxis  $a$  normalized by the initial radius  $R = D/2$ , with the corresponding parameters described in Table 1. The timestep at which the drop first touches the solid surface is also highlighted with an open circle.

**Table 1**

Relevant dimensionless parameters in the case of pre-impact deformation studies in high speed conditions, matching in drop diameter to a subset of the studies performed by Sor and García-Magariño (2015).

$D$ [m]	$Re = \rho_l U_\infty D / \mu_l$	$We = \rho_l U_\infty^2 D / \sigma$	$Oh = \sqrt{We} / Re$	$Ca = \mu_l U_\infty / \sigma$	$St = \mu_g / (\rho_l D U_\infty)$
$128 \times 10^{-6}$	8653.717	10936.183	0.012	1.263	$1.803 \times 10^{-6}$
$362 \times 10^{-6}$	24473.794	30928.893	0.007	1.263	$6.376 \times 10^{-7}$
$634 \times 10^{-6}$	42862.943	54168.282	0.005	1.263	$3.640 \times 10^{-7}$
$1048 \times 10^{-6}$	70852.309	89539.999	0.004	1.263	$2.202 \times 10^{-7}$

secondary structures around the edges which ultimately rupture from the main shape and break off into smaller droplets prior to impact. It should be noted that there is a difference in timescales when comparing the experimental and computational results; in the experimental data the deformation takes place over a distance of several hundred drop diameters, whereas in all computational results this evolution takes place within the prescribed distance of roughly 20 initial drop diameters. The flow field and its extensional nature is effectively scaled down to the size of the computational box.

From a quantitative perspective, for comparison purposes we use the same semiaxis deformation metric  $a(t)/R$  in Fig. 3(c) to uncover an excellent agreement with the experimental data. We mark the time of impact with an open circle and note that the obtained values are within 10% of their experimental counterparts, while the evolution of this measurement in time also shows the same features. Notably, for the larger drop we plot the full extent of the liquid volume (accounting for the shedding of secondary droplets). If these are to be excluded, at a distance of half a diameter above the solid surface, the deformation is found to be 1.36, 1.72 and 1.85 for the  $362 \mu\text{m}$ ,  $634 \mu\text{m}$  and  $1048 \mu\text{m}$  drops, respectively, with approximately 1.3, 1.7 and 1.94 being the equivalent values in the experiment. The inclusion of secondary drops becomes visible around  $t \approx 15$  in both cases and causes an increase in this metric to just below 2.0 and 3.0 for the two largest droplets, indicating the complexity of the flow in the respective regimes as the drops approach the surface.

The computational framework developed here can be used to access information on the flow field and drop shape at distances very close to the surface that are beyond the frame-restricted capabilities of current powerful video technology. Consequently, we consider the case of a smaller drop of initial diameter  $D = 128 \mu\text{m}$  and find very small deviations from the imposed shape during its entire evolution. A small initial flattening of the shape into an oblate spheroid suffers corrections prior to impact and ultimately impinges almost undeformed.

For completeness, all four cases are illustrated in Fig. 4 at the last computed timestep before touchdown, with the last  $D = 1048 \mu\text{m}$  case being placed side-by-side with its experimental counterpart. For the smallest drop, deformation is hardly visible (as confirmed by Fig. 3(a)), with an approximately spherical liquid volume impinging onto the surface. A strong flattening of this shape with the beginning of breakup features becoming visible around the edges takes place for slightly larger drops and this ultimately leads to progressively smaller liquid fragments/drops being shed from the sides. In the largest drop volume case, the cloud of droplets behind the main liquid volume becomes visible and resembles the experimental result.

In what follows we focus on the impingement process itself and in particular on the spreading or splashing characteristics of the flow, as well as the associated secondary drop formation and dynamics.

#### 4.2. Post-impact dynamics

Once the drop approaches the region very close to the wall, the gradually thinner air film below is forced to move away laterally and the pressure underneath the droplet continues to grow until impact takes place. We note the presence of either a single or multiple air bubbles entrained under the surface. In the classical context with a quiescent air flow and small to moderate impact velocities, the size and evolution of the air bubble is well studied, and its effect on the splashing process itself has been shown to be negligible (Riboux and Gordillo, 2014). In the present case however, there are two fundamental differences from the traditional impact problem due to the very high impact velocity, as well as the strong pre-impact drop deformation, particularly in the oblique impingement cases. In the first instance and on the basis of Fig. 5, we will provide a qualitative assessment of the results. The studied parameter space consists of the two cases outlined in Table 2 of normal impact and oblique impact at  $60^\circ$ , and four different drop diameters, producing eight studies in total. The time sequence of top



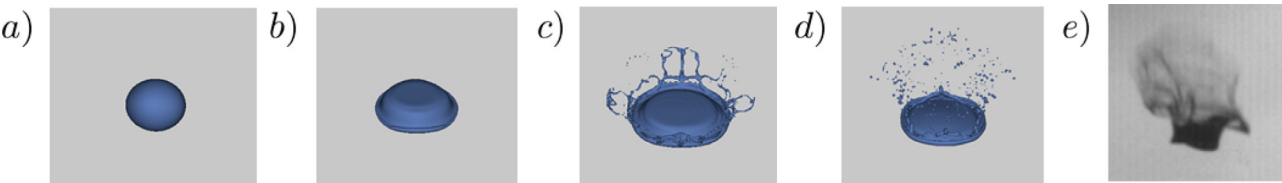


**Fig. 4.** Initially spherical droplets of diameter (a)  $D = 128\text{ }\mu\text{m}$ , (b)  $D = 362\text{ }\mu\text{m}$ , (c)  $D = 634\text{ }\mu\text{m}$ , and (d)  $D = 1048\text{ }\mu\text{m}$ , at the moment of impact onto a flat solid surface, having been deformed by the background stagnation point flow. The smallest drop retains its shape, while the edges of the largest drop break up into a large number of secondary droplets even before impact. This compares favourably to e) previous experimental investigations of drop deformation prior to impacting a moving solid body ( $D_{\text{exp}} = 1048\text{ }\mu\text{m}$  as well) by Vargas et al. (2012). The last image is reproduced with permission by Instituto Nacional de Técnica Aeroespacial.

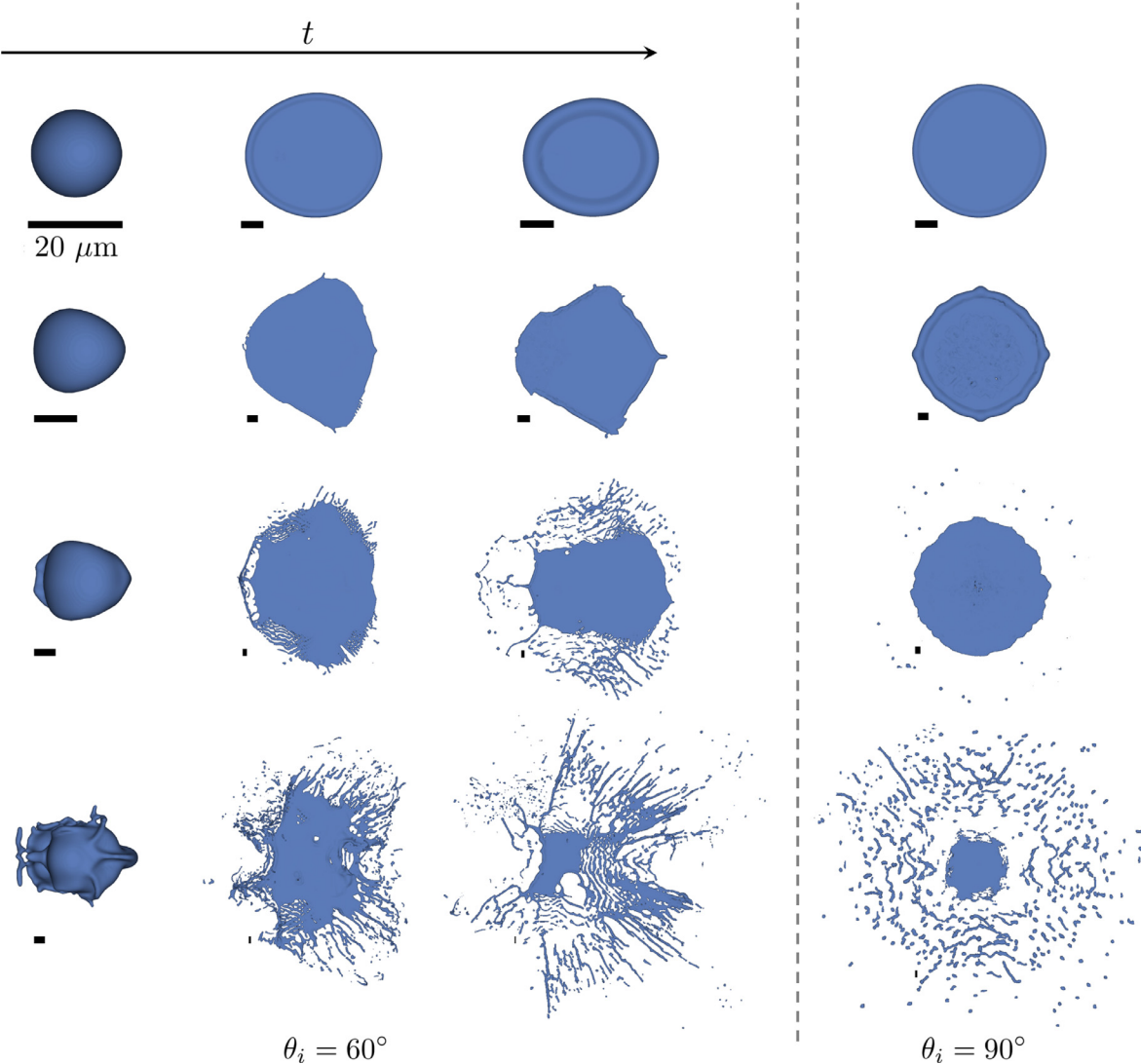


**Fig. 5.** Splashing dynamics for drops of sizes  $D = 20, 52, 111$  and  $236\text{ }\mu\text{m}$  (each row represents a different drop size, with the complete list of parameters defined in Table 2) at an angle of incidence of  $\theta_i = 60^\circ$ . The left column illustrates the drop shapes as their center of mass is at  $y = D$  above the surface, the images in the second column are plotted at the dimensionless timestep at which the drop illustrated on the top row (smallest drop, with initial diameter  $D = 20\text{ }\mu\text{m}$ , and relatively regular spreading behaviour) reaches its maximum spread  $t_s^{\text{max}}$ , while the third column shows the drop shapes ten time units later, once either retraction or more pronounced splashing has occurred. The rightmost column is used to visualise the splashing for the  $\theta_i = 90^\circ$  impact case at  $t_s^{\text{max}}$ .

Table 2					
Relevant dimensionless parameters in the case of long-time drop impact direct numerical simulations in high speed conditions, matching in median volumetric diameter to a subset of the studies performed by Papadakis et al. (2003). The splashing parameter $K = \text{We}\sqrt{\text{Re}}$ varies between $6.283 \times 10^4$ and $2.547 \times 10^7$ .					
$D\text{ [m]}$	$\text{Re} = \rho_l U_\infty D / \mu_l$	$\text{We} = \rho_l U_\infty^2 D / \sigma$	$\text{Oh} = \sqrt{\text{We}} / \text{Re}$	$\text{Ca} = \mu_l U_\infty / \sigma$	$\text{St} = \mu_g / (\rho_l D U_\infty)$
$20 \times 10^{-6}$	1352.143	1708.779	0.031	1.263	$1.154 \times 10^{-5}$
$52 \times 10^{-6}$	3515.573	4442.824	0.019	1.263	$4.438 \times 10^{-6}$
$128 \times 10^{-6}$	8653.717	10936.183	0.012	1.263	$2.079 \times 10^{-6}$
$236 \times 10^{-6}$	15955.291	20163.588	0.009	1.263	$9.779 \times 10^{-7}$

views of the liquid drop on the left hand side of Fig. 5, illustrates the drop shape at three key times in its evolution, namely:

- (i) when the center of mass of the drop lies one initial diameter above the surface (left column);
- (ii) when the drop reaches its maximum spread on the surface and before retraction under capillary forces takes place (middle column);
- (iii) ten time units later, which serves as an indication of how the longer timescale of the impact develops into either retraction for the smaller drops or violent rupture and splashing for the larger drops (right column).

For the  $90^\circ$  impact case we concentrate on the second of the above time instances, namely when the smallest drop reaches its maximum diameter – results are shown in the right hand side column of Fig. 5. In each image a reference lengthscale of  $20\mu\text{m}$  is added as a visual aid to the extent of the drop atomisation (or lack thereof).

The smallest drop size (initial diameter  $D = 20\mu\text{m}$ ) impingement is characterised by inconsequential pre-impact deformation with the approximately spherical shape retained up to very near the time of impact, followed by a strong spreading motion in a highly inertial regime, finally followed by retraction due to surface tension. Intriguing corner-type features emerge particularly for the oblique impact cases due to the directionality of the impact, which will be discussed in detail in subsequent paragraphs. Referring to the oblique impact scenario, the asymmetry becomes more visible for medium sized drops (at the order of  $100\mu\text{m}$  in initial diameter) prior to impact and particularly after impact as fluid volumes have sufficient momentum to overcome surface tension and push outside the typical nearly circular contour, instead spreading laterally outward towards the front of the drop. The dynamics is however still dominated by one large fluid volume from which small secondary drops are ejected as the drop increases in size. We underline that the imposed angle of incidence has a clear influence on the angle and extent of lateral spread of the liquid mass. The largest drops ( $D = 236\mu\text{m}$ ) experience violent splashing, with visible liquid threads forming in the forward and laterally outward directions as the fluid mass disintegrates into hundreds of droplets. Similar features are observed in the normal impact case in terms of fragmentation, with traditional spreading motion transitioning to azimuthal instabilities, followed by a rupture of the liquid rim into small drops, but with a main fluid mass still intact near the impact site. Ultimately a violent fragmentation breaks up the liquid volume into thin filaments near the surface, and numerous secondary drops are advected away from the impact region under the influence of the background flow.

Conducting a systematic analysis of the drop's morphology during the early and intermediate stages of the impact is most accessible for the smallest drops (below several tens of microns in initial diameter, top row of Fig. 5, when no splashing occurs), where early and very recent analytical results are available for comparison when  $\theta_i = 90^\circ$ . Following this baseline, the generalisation to the predominantly three-dimensional effects of the asymmetric impact are best constructed. Even in the normal impact case however, the presence of the non-quiescent air flow at high speeds is anticipated to produce some modifications in the standard metrics surrounding the characterisation of the impingement process, which will be emphasised in the following paragraphs.

In order to aid future comparisons, in Fig. 6 we define several quantities of interest, namely the time-dependent drop diameter in the  $x$ -direction  $D_x(t)$  (the direction of impact for the non-normal incidence cases), the drop diameter in the transverse  $z$ -direction  $D_z(t)$ , as well as the height of the drop near its center of mass  $h_f$ . The first two metrics are best observed from the top view ( $x-z$

plane) presented in the top part of panel a, while a cut through the  $x-y$  plane provides information on the minimum thickness of the film. The entrapment of a small air bubble due to impact cushioning, results in a small variation in the drop's curvature just above this feature, which is why for the relevant local minimum we select a point where this local adjustment is negligible. Several notable studies (see Introduction) have addressed the topic of the maximum spread  $D_m$  of the drop in normal impact conditions, with the recent investigation of Wildeman et al. (2016) chosen as reference here. Plugging our parameters into their main result, we find  $D_m \approx 4.112$ , which compares very well with the computed value for  $\theta_i = 90^\circ$  in Fig. 6(c). Symmetry in this case is preserved and we find  $D_x^{\text{max}} = D_z^{\text{max}} \approx 3.9$ , which alongside the good agreement also indicates that the surrounding flow has a limited influence on the maximum spread.

As the angle of incidence is decreased down to  $\theta_i = 30^\circ$ , the flow speed in conjunction with the increasingly pronounced directionality of the impact enables the liquid mass to advance towards the front side (in the  $x$ -direction) of the impacting drop, pushing more strongly towards the front edge and increasingly distorting it in this direction. Fig. 6(c) indicates this monotonic increase in  $D_x^{\text{max}}$  and decrease in  $D_z^{\text{max}}$  as  $\theta_i$  is reduced, with the final aspect ratio being measured at almost a factor of two. We point out that in this regime the drop is also subjected to a stronger air flow as it lies further away from the dividing streamline and the background flow velocity has an increased magnitude. For illustrative purposes, in Fig. 6(b) we expand on how the maximum diameter values are obtained in the asymmetric cases, with the two diameters  $D_x(t)$  and  $D_z(t)$  being shown throughout their evolution for an angle of incidence  $\theta_i = 60^\circ$ . The dynamics in the  $x$ -direction is chosen as reference, as this is the dominant motion due to our choice in impact directionality. The value of  $D_z^{\text{max}}$  is then defined as the value of  $D_z(t_x^{\text{max}})$ , where  $t_x^{\text{max}}$  is the timestep at which  $D_x$  reaches its maximum, despite it not necessarily being the highest absolute value in the  $z$ -direction. The figure shows negligible deformation up to the time of impact  $t \approx 20.0$ , followed by a sharp increase in diameter in both directions but more strongly in  $x$ , with the rim finally retracting under the effect of surface tension from all directions. The reference values (see vertical dashed line) derived from similar studies of each incidence angle are then used to construct Fig. 6(c).

Another key morphological metric we consider is the minimum film height, as extracted near the drop center, sufficiently far away from the entrapped bubble. In the normal impact case and in the strong inertial regime described here, Eggers et al. (2010) estimate this thin film height to reach a minimum  $h_f/R \approx \text{Re}^{-2/5}$ , which would give  $h_f \approx 0.028$  in our case. This is the height at which the thinning film reaches the liquid boundary layers within the drop itself and ceases its decrease. The result obtained in our investigation is  $h_f \approx 0.033$  and we found no evidence of significant variation as a result of modifying the angle of incidence. The very slight overestimation is perhaps counterintuitive given that the fast air flow pushing from above would be expected to enhance the thinning effect. We note that even at these small lengthscales the mesh is sufficiently fine with several gridpoints spanning the thin film region; changes in the resolution did not result in meaningful changes of this value.

One of the most salient features of the drop impact in the modelled high speed regime is the emergence of a corner-type feature near the advancing front of the spreading liquid mass; this feature becomes highly prominent, particularly as the angle of incidence  $\theta_i$  is  $60^\circ$  or lower. Above the respective angle, normal impact is characterised by approximately axisymmetric behaviour, while in slightly oblique impacts ( $\theta_i \approx 70^\circ - 80^\circ$ ) the footprint can be described as elliptical, although a slight symmetry-breaking tilt to the front becomes observable on the lower side of this range. A

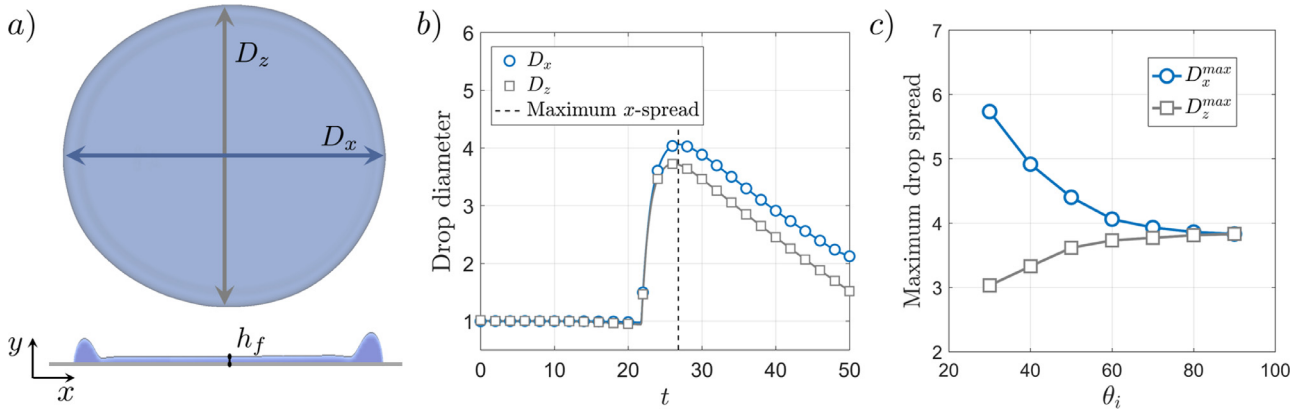


**Fig. 6.** Spreading dynamics of microdroplets with an initial diameter of  $D = 20 \mu\text{m}$  at angles of incidence ranging from  $30^\circ$  to  $90^\circ$ . (a) Top view schematic of the spreading diameter in the  $x$ -direction (the impingement direction) and the  $z$ -direction, as well as the minimal film thickness  $h_f$  (in side view below), for an angle of incidence of  $\theta_i = 60^\circ$ . (b) Evolution in time of the spreading and later retracting liquid drop for the  $60^\circ$  impingement angle case. (c) Summary of the maximum spread in both  $x$  and  $z$  for a collection of angles of incidence, indicating the transition from symmetric spreading to a strongly asymmetric final shape in the direction of impact.

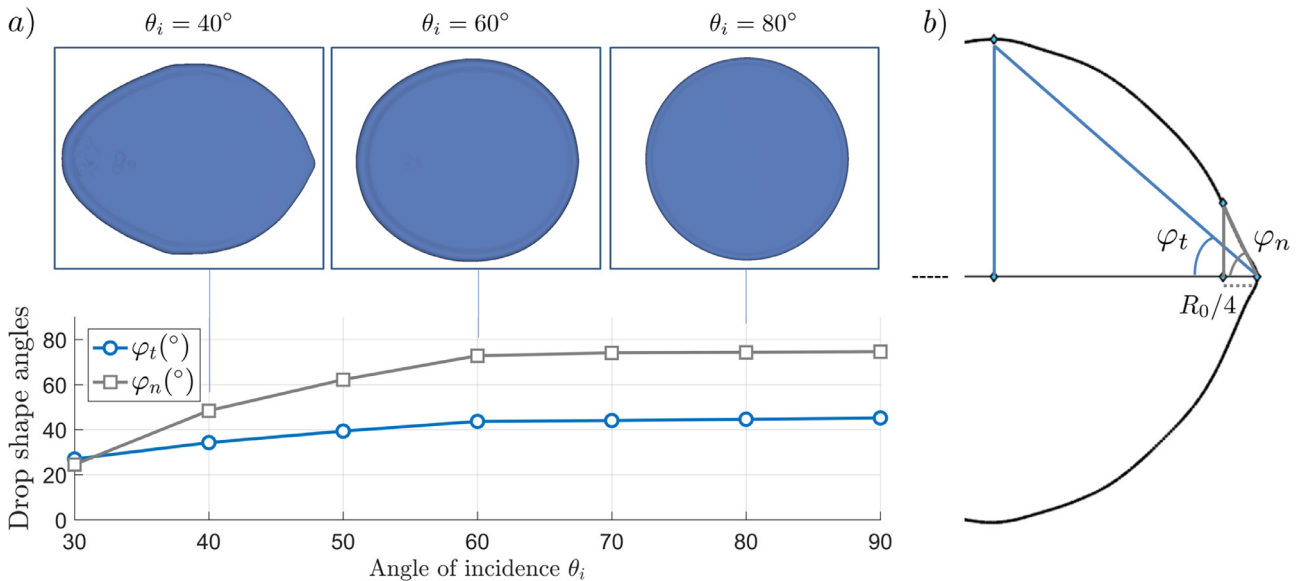


**Fig. 7.** (a) Characterisation of the geometric feature arising at the leading (front) side of the drop due to the oblique impact. Angle  $\varphi_t$  is measured from the most advanced point of the drop in the direction of impact to the maximum in the spread in the perpendicular direction of the same plane, while  $\varphi_n$  represents the more local feature arising at  $0.25R_0$  behind the front, where  $R_0$  represents the initial drop radius. Both angles are defined in panel (b), while the three insets present top views of the drop shape at the moment of maximum spread in the  $x$ -direction, the timestep at which all the angles in the figure are calculated.

comprehensive analysis of the corner-type property has been performed for angles varying in the range  $10^\circ \leq \theta_i \leq 90^\circ$  and small drop size (initial diameter  $D = 20 \mu\text{m}$ ), and the results are given in Fig. 7. Herein we track the evolving drop shape from above, and concentrate on the moment where its spreading diameter reaches its maximum value for each of the particular cases. Two angular metrics are then defined as illustrated on the right hand side of Fig. 7:  $\varphi_t$  (angle from the tip of the advancing front in the impingement  $x$ -direction to the top part of the drop, the maximum in the  $z$ -direction) is a more global measure of the deformation, whereas  $\varphi_n$  is a local measure of the corner angle near the tip of the advancing front, defined by a triangle whose base is fixed to be a quarter of the initial radius  $R/4$ , as shown in the figure. We emphasise that while the discussed feature is called a corner (or of corner-type) throughout this subsection, the shape would be more accurately described as an apparent corner, since locally near the tip of the advancing front surface tension always induces a smoothing of the shape.

The progressively more stretched shape of the drop, as well as the evolution near the tip of the advancing front capturing the

corner-type feature itself are both embedded in the above quantities, which are presented at the bottom of Fig. 7, with examples of the underlying drop shapes depicted in the row above for  $\theta_i = 40^\circ, 60^\circ$  and  $80^\circ$ . In the intermediate case small distortions of the liquid rim are already visible, while at  $40^\circ$  a pronounced outgrowth near the advancing front selected by the direction of impact is clearly identifiable. Due to the preserved axisymmetry, at  $\theta_i = 90^\circ$  we compare the numerical results with simple predictions. We naturally expect  $\varphi_t \approx 45^\circ$  and based on the maximal spreading radius described in Fig. 6(c), the definition of the angle  $\varphi_n$ , as well as using basic trigonometry, we estimate  $\varphi_n \approx 75^\circ$ . We recover  $\varphi_t = 44.93^\circ$  and  $\varphi_t = 74.76^\circ$  by analysing the data, which is well aligned with the anticipated axisymmetric evolution. Both angle measurements are expected to decrease in oblique impact scenarios, with the elongation of the liquid shape gradually reducing their values as  $\theta_i$  decreases. This is indeed the case, with a smooth monotonic variation in  $\varphi_t$  finalising at approximately  $22^\circ$  for the  $\theta_i = 30^\circ$  impingement case. The local angle  $\varphi_n$  naturally begins at a much higher value, but again, as the impingement angle  $\theta_i$  decreases, the deformation of the spreading drop is enhanced

and this results in a steady decline from  $\varphi_n \approx 75^\circ$  for the normal impact case down to  $\varphi_n \approx 25^\circ$  at  $\theta_i = 30^\circ$ . The slope characterising this decrease becomes markedly larger in absolute value below  $\theta_i = 60^\circ$ . Note however that due to the shape irregularity this definition becomes less practical for angles below  $\theta_i = 50^\circ$ , as high variation is induced depending on the choice of distance defining  $\varphi_n$ . In particular, the top left hand side inset in Fig. 7 reveals the formation of a small finger-like extension that becomes smoothed out under surface tension. The strongly varying curvature of this shape near the tip makes it difficult to design a universally useful local metric to describe the corner, which is why the choice of a distance of  $R_0/4$  behind the advancing tip should in some sense be interpreted with an embedded variation, as would any other choice.

Finally, a physical interpretation of the corner formation process is proposed as a combination of two different mechanisms, one related to the background flow, the other to the liquid movement itself. In the latter case, during the spreading motion liquid pushes into the front of the rim in a preferential direction given by the progressively more oblique impact as defined by  $\theta_i$ . There is sufficient inertia to drive more liquid mass towards the advancing front, however this is insufficient to overcome surface tension in the lateral direction due to the relatively small size of the drops. As such, the liquid that accumulates in the rim in the lateral regions is also steered towards the front of the drop, where at the meeting point the conditions for a localisation of the interfacial shape into a corner are met before surface tension relaxes this feature. At the same time, high speed air is pushing from above in the same direction as the primary impacting motion, further guiding liquid into this front region. This becomes far more evident for the lower impingement angles in which the drop spreads on the surface in a region several diameters away from the flow stagnation point and as such the local shear forces become gradually stronger, supporting the complete manifestation of the observed corner at the advancing front of the spreading drop.

For impingement angles lower than  $\theta_i \approx 30^\circ$ , we find entirely different phenomena captured in Fig. 8. The near-glancing incidence of the drop, coupled with a more uni-directional background air flow, both contribute to a pinch-off near the advancing front of the liquid volume, as opposed to the creation and subsequent relaxation of a corner-type feature. For most of its development, the region near the front of the drop advances on top of a very thin liquid film, with the bulk of the liquid mass eventually catching up with significant horizontal velocity (used to colour the liquid interface in each figure in Fig. 8). The advancing front of the strongly elongated shape retains sufficient inertia to eventually detach from the surface and subsequently break off into several small liquid drops that progress at very high speed towards the edge of the finite computational domain, with the majority of the fluid quantity retained on the solid surface. One of the additional causes underlying the observed filamentation is that the drop lands further away from the global stagnation point in the background flow, implying that locally the flow is predominantly moving in the direction of the spreading in the front, promoting the lateral movement as opposed to pushing down onto the liquid.

Having discussed at length the rich features already appearing in the impact of the smallest drops, we proceed to a quantitative study of the splashing dynamics throughout the entire duration of the direct numerical simulations for the full range of drop sizes considered; these results are summarised in Fig. 9. Recall that the drops are initialised at  $t = 0$ , impacting the surface at  $t \approx 20.0$  and engaging in either spreading motion or generation of secondary droplets being tracked over 80 subsequent dimensionless time units. Detailed results are presented for the asymmetric case with an angle of incidence  $\theta_i = 60^\circ$  and four different droplet sizes ranging from  $20 \mu\text{m}$  to  $236 \mu\text{m}$ .

Focusing on the left panel of Fig. 9, we notice the effect of initial drop size on the formation and break-up of secondary drops. The smallest drop follows the described spreading and retraction motion detailed earlier in Section 4.2 and no secondary drops are ejected from the surface. Instead, a steady spherical cap solution is observed during the final stages. At intermediate sizes, but still below an estimated  $100 \mu\text{m}$  threshold, small drops detach from the edges of the rim in all directions however with a stronger preference towards the direction of impact, with approximately 20–30 secondary droplets being swept away by the air flow and advected towards the lateral outflow boundaries; a few re-impinge onto the surface and remain at the respective locations. For the largest droplets of initial diameter  $D = 111 \mu\text{m}$  and  $D = 236 \mu\text{m}$ , a violent splashing motion ensues (also visible in Fig. 5), with several hundred very small drops moving away from the impingement region. As expected, due to the larger drop size the effect of surface tension is weaker and break-up into progressively smaller liquid fragments is more pronounced. In such cases, even the secondary droplets are subject to subsequent break-ups, with a minimum size being again restricted by surface tension. We have made extensive verifications of the selected grid refinement and minimum cell size in order to restrict numerical artefacts at this level. In fact, the final resolution for these studies was partly selected in light of a convergence to a minimal secondary drop size captured by our simulations. We note, however, that the selective droplet removal procedure performed primarily to avoid instabilities around the boundaries, does affect the secondary droplet count, with some of the smallest droplets ejected as part of the prompt splash away from the surface at very high speed being removed from the finite computational domain within several time units after the impact.

The size and position of each individual drop is tracked after impact and hence statistical information on the secondary drops is compiled and studied dynamically. Two particular points in time have been selected for visualisation purposes on the right hand side of Fig. 9, which represent the early post-impact stage when the maximum number of secondary drops is found in the domain ( $t_1$ ), followed by the point in time halfway through the evolution at  $t = 50.0$  when the main body of fluid no longer ejects secondary drops in the impact region and the secondary drops are airborne ( $t_2$ ). Both of these apply to the case of the largest  $D = 236 \mu\text{m}$  initial diameter drop, selected due to the impact and splash producing the richest secondary drop dataset.

Once the impact has taken place and sufficiently many secondary drops have formed, the volumes of these liquid fragments follows an approximately log-normal distribution (see detail at  $t_1$ ), centred around a mean of  $10^{-4}$  relative to the volume of the initial drop. If assumed to be spherical (which is seldom the case) this translates into droplets with a radius of  $1/20$  relative to the radius of the initial drop. As further fragmentation takes place due to the interaction between the fast movement of the drop and the surrounding air boundary layer flow, a second local maximum becomes prominent, with tens of drops with volumes of the order of  $10^{-6}$  relative to the initial volume being present far away from the impact area. Under the action of surface tension, these drops are often more regular (spherical) in shape if still airborne, with some of them re-impinging far away from the impact region and becoming spherical caps as in the case of the previously studied  $D = 20 \mu\text{m}$  initial diameter drops. In fact, the distribution highlighted at  $t_2$  in Fig. 9 also includes the minimum droplet volume captured within this computation, which is found to be of just less than  $10^{-7}$  or of a radius of  $1/200$  relative to the initial drop – just above  $1 \mu\text{m}$  in dimensional terms (recall the initial drop diameter is  $D = 236 \mu\text{m}$  in this numerical experiment).

The full evolution of the secondary drop size distribution in this case is illustrated with two different visualisation techniques in Fig. 10. We are concentrating on the case of angle of incidence



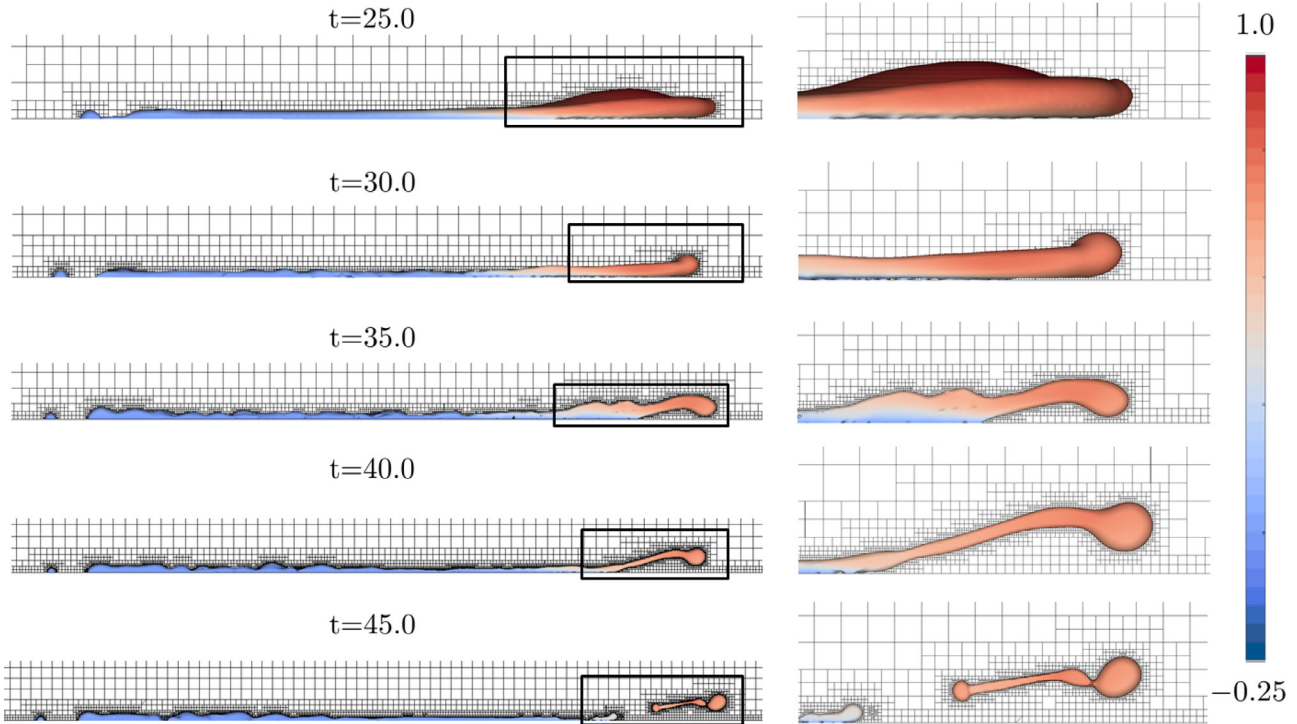


**Fig. 8.** Side view ( $x-y$  plane) of the late time impingement dynamics of a  $D = 20 \mu\text{m}$  drop at an angle of  $\theta_i = 10^\circ$ , resulting in the break-up of a liquid volume in the leading region. The panels on the right illustrate a magnification of this area. The interface is coloured in the magnitude of the horizontal velocity at the respective points, while the adaptive grid underlying each timestep is also shown. For reference, the smallest grid cell measures approximately  $0.39 \mu\text{m}$  in dimensional terms.

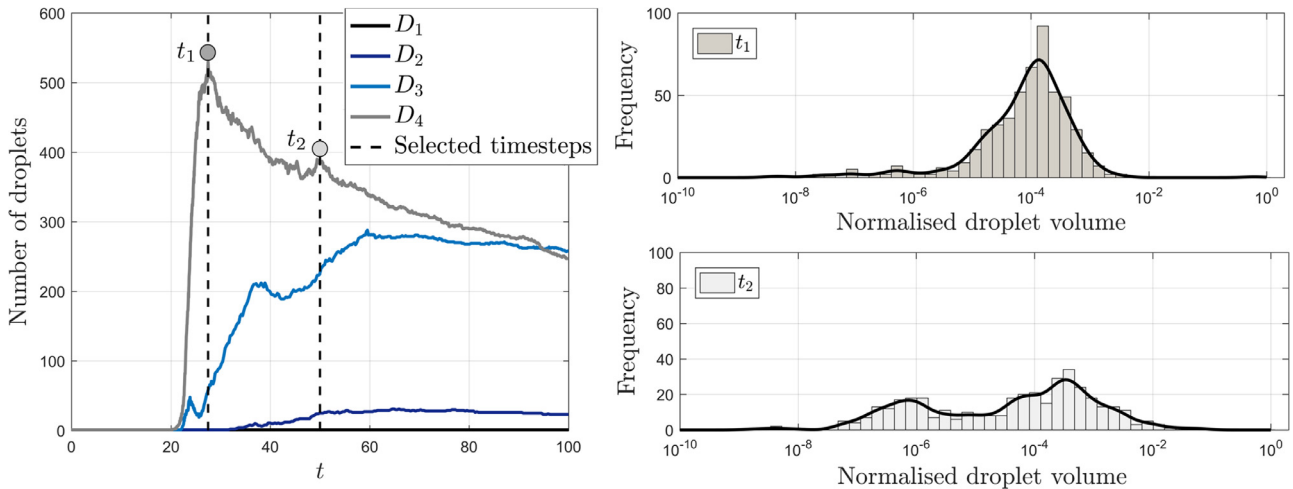


**Fig. 9.** Secondary droplet ejection characteristics as a result of spherical drops of initial diameter  $D = 20, 52, 111$  and  $236 \mu\text{m}$  impinging onto a solid surface at an angle of incidence  $\theta_i = 60^\circ$ . Evolution of the number of droplets in time for each case (left), with the two panels on the right indicating the secondary drop size distribution (normalised by the initial droplet size) for the  $236 \mu\text{m}$  drop at the two different times,  $t_1$  and  $t_2$ , highlighted in the left panel.

$\theta_i = 60^\circ$ , however we have found the qualitative behaviour described below to be consistent with variation in  $\theta_i$ . The observed log-normal distribution evolves (with the number of drops increasing, but the structure being retained) over roughly 15 time units. At this stage ( $t \approx 50$ ), most drops in the system appear to follow one of two general tendencies:

1. the larger drops in the distribution are the ones which are detached from the main liquid mass but lie on the solid surface (after early dynamics or later re-impingement) as approximately spherical caps. After they reach this configuration they will only increase in size as a result of coalescence with neighbouring spherical caps or incoming smaller secondary drops that re-impinge onto the surface. This region, the right hand side local maximum centered around  $10^{-3}$  in normalised volume) remains relatively steady in both number of drops and extent of variation.
2. the fragmentation process around the left hand side second local maximum in the distribution (with mean of approximately  $10^{-7} - 10^{-6}$ ) is rich and spans roughly two orders of magnitude in normalised volume. These are primarily airborne drops that continue to travel, break up or coalesce as a result of the interaction with the background air flow.

Rather remarkably, we find that the separation between the two types of drops (the two local maxima in the distribution) is relatively well preserved when changing both initial drop size and angle of impingement. To confirm this, however, these preliminary results will be extended over wider parameter ranges and flow conditions in future work that is currently under way.

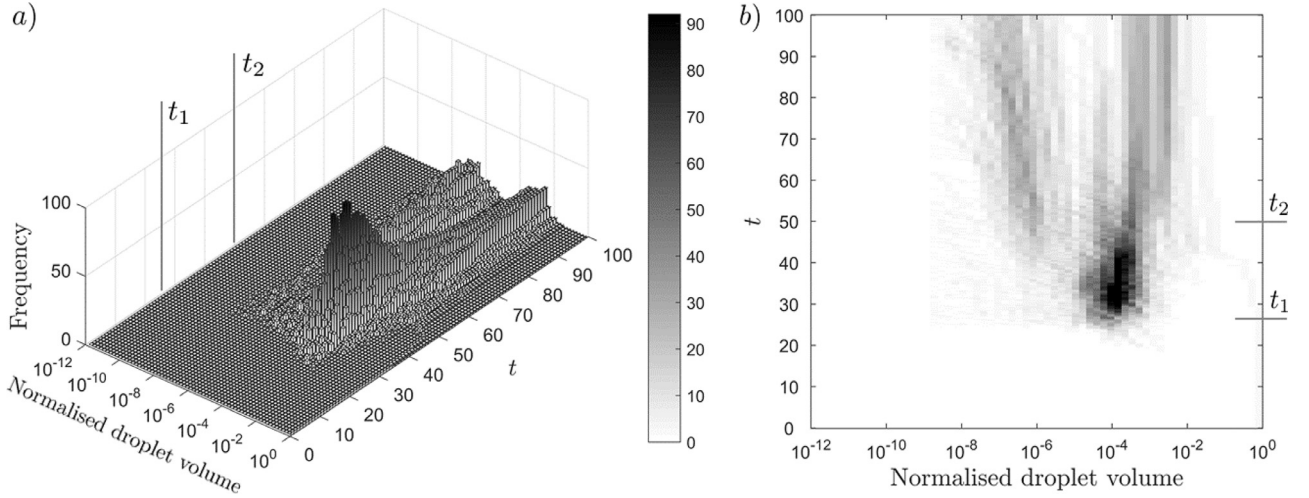


**Fig. 10.** Secondary droplet size distribution evolution characteristics for the largest drop in the test batch summarised in Table 2 and indicated as  $D_4$  in Fig. 9, impinging onto a solid surface at an angle of incidence  $\theta_i = 60^\circ$ . (a) Left panel: three-dimensional view, with timesteps  $t_1$  and  $t_2$  detailed in Fig. 9 marked with vertical bars. (b) Right panel: top view of the same dataset in the form of a contour plot.

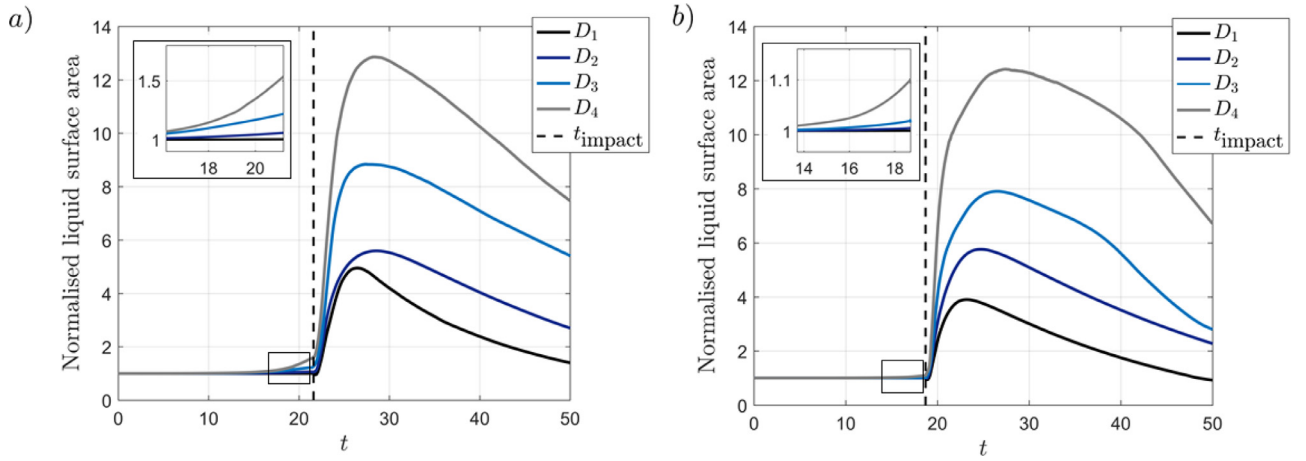


**Fig. 11.** Normalised liquid-gas surface area as a function of time for four different drop sizes (summarised in Table 2) and two impingement angles: (a)  $\theta_i = 60^\circ$  and (b)  $\theta_i = 90^\circ$ . The insets in each subplot concentrate on the evolution of the surface area during the five time units just before the moment of touchdown, marked by a vertical black dashed line in the full scale images.

The same type of data analysis as presented above may be useful in furthering our understanding of the dynamics very close to the splashing threshold, with possible comparisons with the work of Riboux and Gordillo (2015) becoming an interesting future line of investigation. In its current form, the high speed regime and presence of the background flow in the model make such direct comparisons difficult, however early calculations indicate that the first drops ejected as part of the splashing process lie encouragingly close to the previously mentioned predictions.

The present work was in part motivated by the question of how extending our understanding of liquid droplets impinging onto solid surfaces in high speed conditions acts as one of the early building blocks in the broader context of icing prevention and aircraft safety and design. As a result of the deformation and splashing dynamics forming the subject of the present work, a useful metric to discuss is the evolution of the liquid-gas surface area, which may in the future be considered in view of coupling to thermodynamic effects. We illustrate our findings for the four cases introduced in Table 2 and two angles of incidence,  $\theta_i = 60^\circ$  and  $\theta_i = 90^\circ$  in Fig. 11. To aid the discussion around the quantitative information, we introduce two simple approximations of what could

be anticipated in light of previously elucidated dynamics and focus on the normal impact scenario for clarity.

For the smallest drops studied ( $D_1$  here), we find that spreading and retracting behaviour is still characteristic and as such we can use a straightforward analogy in terms of a flat cylinder of appropriate radius and height to estimate the corresponding surface area. In particular, considering the time of maximum spread  $t_s^{\max}$ , we find a value of the resulting  $D_x^{\max} \approx D_z^{\max} \approx 3.9$  (see Fig. 6(c)). Assuming (and having verified that) volume conservation holds, we find an approximate height for the cylinder, which in this case is roughly  $1/24$ . As we do not account for the bottom of the cylinder (the side adhering to the solid surface), the adjusted formula for surface area (accounting for the top surface and the side) gives a normalised result  $S_1^{\max} \approx 3.83$ , in excellent agreement with the corresponding maximum in Fig. 11(b). Now looking to the other end of the spectrum i.e. the largest drops considered in which case strong splashing is observed, the drop size distributions in Fig. 9 indicate that most of the drops have volumes with means of either  $10^{-3}$  or  $10^{-6}$  relative to the initial drop volume. Accounting again for conservation of volume, we would anticipate the normalised surface area to vary between 10 and 100 should

we naively assume all drops to be airborne and perfectly spherical. Instead we of course have a combination of these drops, many of which are also on the surface (with the area in contact with the surface not counted), effects which would all bring our estimate closer to the former value of  $S_4^{\max} \approx 10$ . For both impingement angles we notice that this estimate does not deviate significantly from the obtained value.

Comparing the surface area evolution for both scenarios, we naturally find an increase with drop diameter, however this increase appears to be much more ordered in the normal impact case in terms of both distance between maxima and profile shapes. It should also be noted that, as the insets present, the pre-impact deformation and hence surface area generated is more pronounced for the case with oblique incidence. Once touchdown occurs, the initial strong increase in surface area is dominated by the spreading mass of liquid in both cases, with fragmenting secondary drops only adding negligible features to the evolution for large initial diameter cases. As soon as a spreading maximum is reached, capillary forces cause smooth retraction for the smaller drops. This is in contrast to the larger drop cases, in which, despite the apparent smoothness of the curves, a closer inspection reveals prominent bumps indicating individual fragmentation or coalescence events for small drops. Ultimately capillary retraction as well as drops exiting the finite computational domain through lateral boundaries lead to a decrease in overall liquid-gas surface area.

While much of our attention is dedicated to modelling and quantifying aspects related to single drop impingement dynamics at high speeds, we emphasise that the produced datasets encoding sizes and locations in space and time of all secondary drops becomes central in determining further re-impingement events and elucidating retention properties in general. From a broader perspective, throughout the present section we have described not only fundamental flow features, but also intricate dynamics and a level of physical detail which is invariably omitted once highly simplified coarse-graining procedures are considered instead. In a practical context, this information may provide an accurate physical foundation for engineering models on larger scales and is the subject of ongoing work in our group.

## 5. Conclusions

In the present work, three-dimensional drop impact at high velocities has been investigated numerically through the use of high accuracy direct numerical simulations in order to advance our understanding of drop deformation and splashing dynamics in an aerodynamic context. A model that encompasses the transition from larger lengthscales of typical engineering applications (of the order of an airfoil chord or nacelle diameter) down to the local impact region, whilst accounting for the surrounding (non-quiet) air flow has been proposed. Using an oblique-stagnation point flow model for the background flow provides a suitable framework for the impinging drop to naturally interact with structures such as the growing boundary layers it would encounter on aircraft surfaces. Pre-impact deformation and break-up is compared to available experiments in the relevant parameter range of  $\mathcal{O}(100)$  m/s impact velocities and  $D = \mathcal{O}(100 - 1000)$   $\mu\text{m}$  diameter drops. The impingement of the smallest droplets is described by a regular spreading motion, while beyond a certain size (estimated to be of approximately 50  $\mu\text{m}$ ), violent splashing is observed. Topological changes such as droplet break-off or coalescence, as well as potential subsequent re-impingement of smaller fragments have been taken into account.

Comparison with existing analytical results is possible for the tractable spreading dynamics of the smallest drops in the tested range (under 50  $\mu\text{m}$  in diameter). Variation in the angle of impingement (not previously performed in this regime) reveals in-

triguing corner-type features at the advancing impact front which warrant further investigation. These emerge as a result of the asymmetric impact pushing more fluid mass in a preferred direction, however with surface tension preventing break-up above a 30° angle of incidence, and the action of the strong background flow induced shear. Below this angle, fluid filaments have been shown to form and detach from the surface near the advancing droplet front, breaking into large droplets and being carried away by the surrounding air flow. For larger drops, splashing and secondary drop ejection is captured numerically in detail and examined in order to advance understanding of the water retention process. The average number of secondary drops resulting from the impact increases with the initial droplet diameter, with their sizes well-represented by a log-normal distribution, with a secondary local maximum emerging as a result of further break-up at the final stages of the simulated dynamics.

These findings provide detailed insight into the highly complex fluid dynamical processes occurring during aircraft flight through high liquid water content regions. The present approach and simulations are a significant advance of standard particle-based methods which are common industrial practice and which rely heavily on semi-empirical arguments. The modelled background air flow provides a reliable local description of the flow in which a full interaction between the air and the liquid is permitted and the deformation of the drops is captured in detail before impact, while the emergence and movement of secondary drops in an active flow region is also treated realistically. Significant efforts have been made in order to ensure a highly accurate resolution of the flow. Nevertheless, we emphasise that these results originate from very intensive and resource heavy computational efforts (both in terms of runtime and data storage and processing requirements). Further advances in this area of research in terms of both algorithms and raw computing power will facilitate more understanding in these difficult conditions, with access to smaller grid sizes, larger domains (the issue of locality) as well as sensitivity to contact angle dynamics, being only a small subset of the possible future directions within this methodology.

In conclusion, this research provides a renewed perspective on the modelling of water catch on aircraft surfaces, with possible ramifications towards other areas involving high speed drop impact, such as inkjet printing, combustion and agricultural sprays. The presented results have shown very favourable agreement with recent experimental and analytical results, where possible, in an incredibly challenging regime, whilst new phenomena and detailed quantification of practical information beyond the capabilities of present video technology and analytical treatments has also been provided. We believe that the proposed numerical framework is a valuable tool not only from the fundamental perspective in the study of drop impact, but also in an engineering context as a means of using scale transition to include detailed physical and fluid-related processes in water retention estimation and associated phenomena such as icing.

## Acknowledgements

The authors acknowledge the support of Innovate UK through the SANTANA (System Advances in Nacelle Technology Aerodynamics, project reference 113001) program. The authors were also partly supported by EPSRC grants [EP/K041134/1](#) and [EP/L020564/1](#). We are grateful to Richard Newman and Hui Yao from Bombardier Aerospace Ltd. for fruitful practical discussions. Finally, we would like to thank the anonymous referees for their insight and thoughtful comments.



## References

- Afkhami, S., Zaleski, S., Bussman, M., 2009. A mesh-dependent model for applying dynamic contact angles to VOF simulations. *J. Comput. Phys.* 228, 5370–5389.
- Agbaglah, G., Thoraval, M.-J., Thoroddsen, S., Zhang, L., Fezzaa, K., Deegan, R., 2015. Drop impact into a deep pool: vortex shedding and jet formation. *J. Fluid Mech.* 764.
- Bartolo, D., Josserand, C., Bonn, D., 2005. Retraction dynamics of aqueous drops upon impact on non-wetting surfaces. *J. Fluid Mech.* 545, 329–338.
- Bilodeau, D., Habashi, W., Fossati, M., Baruzzi, G., 2015. Eulerian modeling of supercooled large droplet splashing and bouncing. *J. Aircr.* 52 (5), 1611–1624.
- Bird, J.C., Tsai, S.S., Stone, H.A., 2009. Inclined to splash: triggering and inhibiting a splash with tangential velocity. *New J. Phys.* 11 (6), 063017.
- Blyth, M., Pozrikidis, C., 2005. Stagnation-point flow against a liquid film on a plane wall. *Acta Mech.* 180 (1–4), 203–219.
- Bragg, M., 1996. Aerodynamics of supercooled-large-droplet ice accretions and the effect on aircraft control. In: *Proceedings of the FAA International Conference on Aircraft Inflight Icing*, 2, pp. 387–399.
- Cheng, M., Lou, J., 2015. A numerical study on splash of oblique drop impact on wet walls. *Comput. Fluids* 115, 11–24.
- Cherdantsev, A.V., Hann, D.B., Hewakandamby, B.N., Azzopardi, B.J., 2017. Study of the impacts of droplets deposited from the gas core onto a gas-sheared liquid film. *Int. J. Multiph. Flow* 88, 69–86.
- Clanet, C., Béguin, C., Richard, D., Quéré, D., 2004. Maximal deformation of an impacting drop. *J. Fluid Mech.* 517, 199–208.
- van Dam, D., Le Clerc, C., 2004. Experimental study of the impact of an ink-jet printed droplet on a solid substrate. *Phys. Fluids* (1994-present) 16 (9), 3403–3414.
- Deng, T., Varanasi, K., Hsu, M., Bhate, N., Keimel, C., Stein, J., Blohm, M., 2009. Non-wetting of impinging droplets on textured surfaces. *Appl. Phys. Lett.* 94 (13), 133109.
- Dorrepaa, J., 1986. An exact solution of the Navier-Stokes equation which describes non-orthogonal stagnation-point flow in two dimensions. *J. Fluid Mech.* 163, 141–147.
- Eggers, J., Fontelos, M., Josserand, C., Zaleski, S., 2010. Drop dynamics after impact on a solid wall: theory and simulations. *Phys. Fluids* (1994-present) 22 (6), 062101.
- Fedorchenko, A., Wang, A., Wang, Y., 2005. Effect of capillary and viscous forces on spreading of a liquid drop impinging on a solid surface. *Phys. Fluids* 17 (9), 093104.
- Fuster, D., 2013. An energy preserving formulation for the simulation of multiphase turbulent flows. *J. Comput. Phys.* 235, 114–128.
- Gent, R., Dart, N., Cansdale, J., 2000. Aircraft icing. *Phil. Trans. R. Soc. A* 358 (1776), 2873–2911.
- Guo, Y., Lian, Y., Sussman, M., 2016. Investigation of drop impact on dry and wet surfaces with consideration of surrounding air. *Phys. Fluids* 28 (7), 073303.
- Hiemenz, K., 1911. Die Grenzschicht an einem in den gleichförmigen Flüssigkeitsstrom eingetauchten geraden Kreiszylinder. *Dinglers Polytech. J. Ph.D. Thesis*.
- Honsek, R., Habashi, W., Aubé, M., 2008. Eulerian modeling of in-flight icing due to supercooled large droplets. *J. Aircr.* 45 (4), 1290–1296.
- Howarth, L., 1951. The boundary layer in three dimensional flow. Part II. The flow near a stagnation point. *Lond. Edinb. Dublin Philos. Mag. J. Sci.* 42 (335), 1433–1440.
- Jalaal, M., Mehravaran, K., 2012. Fragmentation of falling liquid droplets in bag breakup mode. *Int. J. Multiph. Flow* 47 (0), 115–132.
- Josserand, C., Thoroddsen, S., 2016. Drop impact on a solid surface. *Annu. Rev. Fluid Mech.* 48, 365–391.
- Jung, S., Hutchings, I., 2012. The impact and spreading of a small liquid drop on a non-porous substrate over an extended time scale. *Soft Matter* 8 (9), 2686–2696.
- Kim, J., 2007. Spray cooling heat transfer: the state of the art. *Int. J. Heat Fluid Flow* 28 (4), 753–767.
- Mandre, S., Brenner, M., 2012. The mechanism of a splash on a dry solid surface. *J. Fluid Mech.* 690, 148–172.
- Marston, J., Zhu, Y., Vakarelski, I., Thoroddsen, S., 2012. Deformed liquid marbles: freezing drop oscillations with powders. *Powder Tech.* 228, 424–428.
- Ming, C., Jing, L., 2014. Lattice Boltzmann simulation of a drop impact on a moving wall with a liquid film. *Comput. Math. Appl.* 67 (2), 307–317.
- Moreira, A., Moita, A., Pano, M., 2010. Advances and challenges in explaining fuel spray impingement: how much of single droplet impact research is useful? *Prog. Energy Combust. Sci.* 36 (5), 554–580.
- Mundo, C., Sommerfeld, M., Tropea, C., 1995. Droplet-wall collisions: experimental studies of the deformation and breakup process. *Int. J. Multiph. Flow* 21 (2), 151–173.
- Papadakis, M., Rachman, A., Wong, S.-C., Bidwell, C., Bencic, T., 2003. An Experimental Investigation of SLD Impingement on Airfoils and Simulated Ice Shapes. Technical Report. SAE Technical Paper.
- Papadakis, M., Rachman, A., Wong, S.-C., Yeong, H.-W., Hung, K., Bidwell, C., 2004. Water impingement experiments on a NACA 23012 airfoil with simulated glaze ice shapes. *AIAA Paper* 565, 1–40.
- Pasandideh-Fard, M., Qiao, Y., Chandra, S., Mostaghimi, J., 1996. Capillary effects during droplet impact on a solid surface. *Phys. Fluids* (1994-present) 8 (3), 650–659.
- Philippi, J., Lagrée, P.-Y., Antkowiak, A., 2016. Drop impact on a solid surface: short-time self-similarity. *J. Fluid Mech.* 795, 96–135.
- Popinet, S., 2003. Gerris: a tree-based adaptive solver for the incompressible Euler equations in complex geometries. *J. Comput. Phys.* 190, 572.
- Popinet, S., 2009. An accurate adaptive solver for surface-tension-driven interfacial flows. *J. Comput. Phys.* 228, 5838.
- Potapczuk, M., Al-Khalil, K., Velazquez, M., 1993. Ice accretion and performance degradation calculations with LEWICE/NS. In: *31st Aerospace Sciences Meeting*, p. 173.
- Rein, M., 1993. Phenomena of liquid drop impact on solid and liquid surfaces. *Fluid Dyn. Res.* 12 (2), 61.
- Riboux, G., Gordillo, J., 2014. Experiments of drops impacting a smooth solid surface: a model of the critical impact speed for drop splashing. *Phys. Rev. Lett.* 113 (2), 024507.
- Riboux, G., Gordillo, J., 2015. The diameters and velocities of the droplets ejected after splashing. *J. Fluid Mech.* 772, 630–648.
- Roisman, I., 2009. Inertia dominated drop collisions. II. An analytical solution of the Navier-Stokes equations for a spreading viscous film. *Phys. Fluids* 21 (5), 052104.
- Rutkowski, A., Wright, W., Potapczuk, M., 2003. Numerical study of droplet splashing and re-impingement. In: *41st Aerospace Sciences Meeting and Exhibit*, p. 388.
- Sawan, M., Carbon, M., 1975. A review of spray-cooling and bottom-flooding work for LWR cores. *Nuclear Eng. Des.* 32 (2), 191–207.
- Schroll, R., Josserand, C., Zaleski, S., Zhang, W., 2010. Impact of a viscous liquid drop. *Phys. Rev. Lett.* 104, 034504.
- Sikalo, S., Tropea, C., Ganic, E., 2005. Impact of droplets onto inclined surfaces. *J. Colloid Interface Sci.* 286 (2), 661–669.
- Sor, S., García-Magariño, A., 2015. Modeling of droplet deformation near the leading edge of an airfoil. *J. Aircr.* 52 (6), 1838–1846.
- Stow, C., Hadfield, M., 1981. An experimental investigation of fluid flow resulting from the impact of a water drop with an unyielding dry surface. *Proc. R. Soc. Lond. Ser. A* 373 (1755), 419–441.
- Stuart, J., 1959. The viscous flow near a stagnation point when the external flow has uniform vorticity. *J. Aerosp. Sci.* 26 (124).
- Tamada, K., 1979. Two-dimensional stagnation-point flow impinging obliquely on a plane wall. *J. Phys. Soc. Jpn.* 46, 310.
- Thoraval, M.-J., 2013. Drop Impact Splashing and Air Entrapment. KAUST Ph.D. Thesis.
- Thoraval, M.-J., Takehara, K., Etoh, T., Popinet, S., Ray, P., Josserand, C., Zaleski, S., Thoroddsen, S., 2012. von Kármán vortex street within an impacting drop. *Phys. Rev. Lett.* 108 (26), 264506.
- Thoroddsen, S., Etoh, T., Takehara, K., 2008. High-speed imaging of drops and bubbles. *Annu. Rev. Fluid Mech.* 40, 257–285.
- Thoroddsen, S., Shen, A., 2001. Granular jets. *Phys. Fluids* (1994-present) 13 (1), 4–6.
- Tilley, B., Weidman, P., 1998. Oblique two-fluid stagnation-point flow. *Eur. J. Mech. B/Fluids* 17 (2), 205–217.
- Tooke, R., Blyth, M., 2008. A note on oblique stagnation-point flow. *Phys. Fluids* (1994-present) 20 (3).
- Tryggvason, G., Scardovelli, R., Zaleski, S., 2011. *Direct Numerical Simulations of Gas-Liquid Multiphase Flows*. Cambridge University Press.
- Tsai, P., Pacheco, S., Pirat, C., Lefferts, L., Lohse, D., 2009. Drop impact upon micro- and nanostructured superhydrophobic surfaces. *Langmuir* 25 (20), 12293–12298.
- Vargas, M., Sor, S., García Magariño, A., 2012. Mechanism of water droplet breakup near the leading edge of an airfoil. In: *4th AIAA Atmospheric and Space Environments Conference*, p. 3129.
- Visser, C., Frommhold, P., Wildeman, S., Mettin, R., Lohse, D., Sun, C., 2015. Dynamics of high-speed micro-drop impact: numerical simulations and experiments at frame-to-frame times below 100 ns. *Soft Matter* 11, 1708–1722.
- Wang, C., 2008. Similarity stagnation point solutions of the Navier-Stokes equations—review and extension. *Eur. J. Mech. B/Fluids* 27 (6), 678–683.
- Wildeman, S., Visser, C., Sun, C., Lohse, D., 2016. On the spreading of impacting drops. *J. Fluid Mech.* 805, 636–655.
- Worthington, A., 1876. On the forms assumed by drops of liquids falling vertically on a horizontal plate. *Proc. R. S. Lond.* 25 (171–178), 261–272.
- Worthington, A., 1908. *A Study of Splashes*. Longmans, Green, and Co.
- Wright, W., 2005. Validation results for LEWICE 3.0. In: *43rd AIAA Aerospace Sciences Meeting and Exhibit*, p. 1243.
- Wright, W., 2006. Further refinement of the LEWICESLD model. In: *44th AIAA Aerospace Sciences Meeting and Exhibit*, p. 464.
- Wright, W., Potapczuk, M., 2004. Semi-empirical modelling of SLD physics. In: *42nd AIAA Aerospace Sciences Meeting and Exhibit*, p. 412.
- Xie, Z., Hewitt, G.F., Pavlidis, D., Salinas, P., Pain, C.C., Matar, O.K., 2017. Numerical study of three-dimensional droplet impact on a flowing liquid film in annular two-phase flow. *Chem. Eng. Sci.* 166, 303–312.
- Xu, L., Zhang, W., Nagel, S., 2005. Drop splashing on a dry smooth surface. *Phys. Rev. Lett.* 94, 184505.
- Yarin, A., 2006. Drop impact dynamics: splashing, spreading, receding, bouncing.... *Annu. Rev. Fluid Mech.* 38, 159–192.
- Yokoi, K., Vadiello, D., Hinch, J., Hutchings, I., 2009. Numerical studies of the influence of the dynamic contact angle on a droplet impacting on a dry surface. *Phys. Fluids* 21 (7), 072102.